Boundary-Layer-Mediated Vorticity Generation in Currents over Sloping Bathymetry

ARJUN JAGANNATHAN,[a] KAUSHIK SRINIVASAN,[a] JAMES C. MCWILLIAMS,[a] M. JEROEN MOLEMAKER,[a] AND ANDREW L. STEWART[a]

[a] *Department of Atmospheric and Oceanic Sciences, University of California, Los Angeles, Los Angeles, California*

(Manuscript received 12 October 2020, in final form 13 March 2021)

ABSTRACT: Current–topography interactions in the ocean give rise to eddies spanning a wide range of spatial and temporal scales. The latest modeling efforts indicate that coastal and underwater topography are important generation sites for submesoscale coherent vortices (SCVs), characterized by horizontal scales of $\mathcal{O}(0.1-10)$ km. Using idealized, submesoscale and bottom boundary layer (BBL)-resolving simulations and adopting an integrated vorticity balance formulation, we quantify precisely the role of BBLs in the vorticity generation process. In particular, we show that vorticity generation on topographic slopes is attributable primarily to the torque exerted by the vertical divergence of stress at the bottom. We refer to this as the bottom stress divergence torque (BSDT). BSDT is a fundamentally nonconservative torque that appears as a source term in the integrated vorticity budget and is to be distinguished from the more familiar bottom stress curl (BSC). It is closely connected to the bottom pressure torque (BPT) via the horizontal momentum balance at the bottom and is in fact shown to be the dominant component of BPT in solutions with a well-resolved BBL. This suggests an interpretation of BPT as the sum of a viscous, vorticity-generating component (BSDT) and an inviscid, "flow-turning" component. Companion simulations without bottom drag illustrate that although vorticity generation can still occur through the inviscid mechanisms of vortex stretching and tilting, the wake eddies tend to have weaker circulation, be substantially less energetic, and have smaller spatial scales.

KEYWORDS: Boundary currents; Topographic effects; Boundary layer; Regional models; Vorticity

1. Introduction

An emerging body of evidence from realistic modeling studies suggests that topographic interactions are a significant source of vertical vorticity generation in the ocean. Among regions where this is seen are the Gulf Stream (Gula et al. 2015), California Undercurrent (Molemaker et al. 2015), Solomon Sea in the southwestern Pacific (Srinivasan et al. 2017), the Gulf of Oman (Vic et al. 2015), and the Alboran Sea region of the western Mediterranean (Capó et al. 2021). In all these studies, the vorticity generated on the topographic slopes evolves, through current separation and shear, centrifugal, or symmetric instability mechanisms, to form a turbulent wake populated by submesoscale coherent vortices (SCVs). Oceanic observations of SCVs with a putative topographic origin include, the Beaufort Sea anticyclones (D'Asaro 1988), the eddying wake past the northern end of Palau (MacKinnon et al. 2019), and most recently, a deep, intense cyclonic SCV in the Arabian Sea (De Marez et al. 2020). SCVs are dynamically important because they can transport mass and dissolved materials over long distances in the ocean (Armi and Stommel 1983; Armi and Zenk 1984; McWilliams 1985; Riser et al. 1986; McCoy et al. 2020) and enhance rates of diapycnal mixing in the thermocline (Dewar et al. 2015; Zhang et al. 2019).

The phenomenology underlying vertical vorticity generation in flow past topography is still being unraveled. D'Asaro (1988) proposed, on the basis of observations of potential vorticity (PV) anomalies in the Beaufort Sea SCVs, that frictional torques which arise during flow–topography interactions have an important role in the generation process. Molemaker et al. (2015) provide a geometric argument, subsequently verified in Srinivasan et al. (2019), to describe how bottom drag acting on slope currents produces a horizontal shear, i.e., vertical vorticity. Employing the framework of the barotropic vorticity equation, defined as the curl of the vertically integrated horizontal momentum equations, Molemaker et al. (2015) and Gula et al. (2015) further show that barotropic vorticity is generated primarily through the action of the bottom pressure torque (BPT) (see also Hughes and De Cuevas 2001; Jackson et al. 2006), with the bottom stress curl not contributing significantly in an integral sense. The apparently contradictory roles of bottom friction and BPT in generating vertical vorticity over slopes remains to be reconciled and will be examined in this study.

In developing a mechanistic understanding of vorticity generation on topographic slopes, we seek to elucidate and quantify how the bottom stress mediates this process. A putative role for the bottom stress needs to in turn be reconciled with the expected occurrence of Ekman arrest on slopes, following boundary stress collapse (MacCready and Rhines 1991). Pursuing an integrated vorticity balance analysis, we explore the dynamics of vorticity generation in flow past an elongated ridge using solutions from idealized, fully three-dimensional ROMS simulations. ROMS is the Regional Oceanic Modeling System. The model setup is detailed in section 2. Figure 1 provides a glimpse of the essential dynamics.

Denotes content that is immediately available upon publication as open access.

Corresponding author: Arjun Jagannathan, ajagannathan@atmos.ucla.edu

DOI: 10.1175/JPO-D-20-0253.1

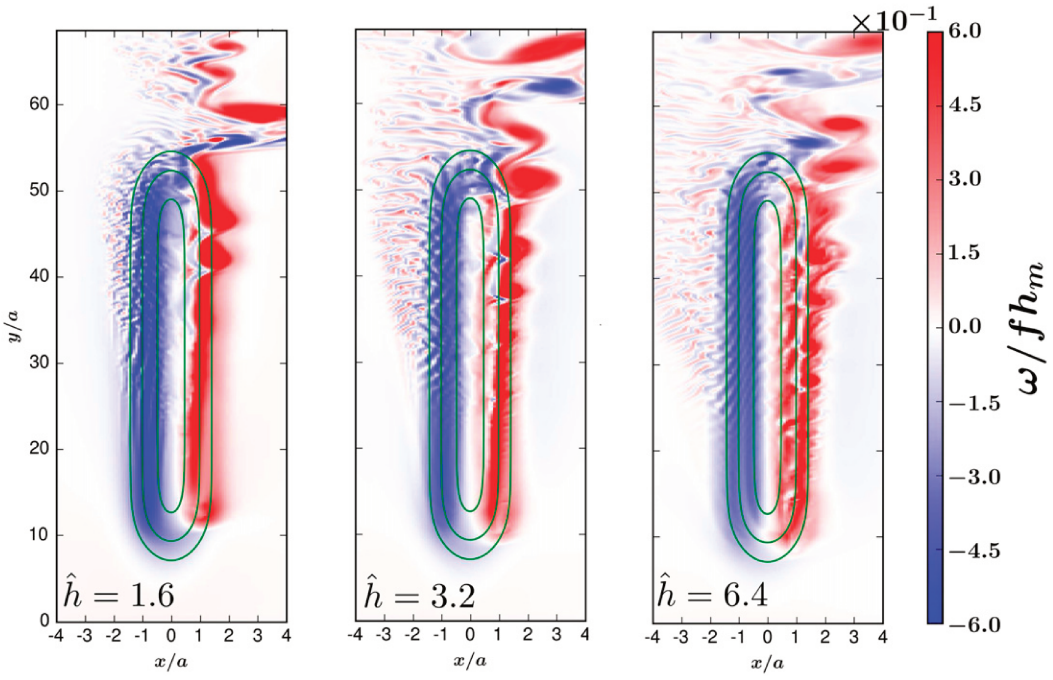

FIG. 1. Snapshots of vertically integrated vorticity, normalized by fh_m for barotropically forced flow past an elongated ridge. The green lines are bathymetry contours at $z = 0.14h_m$, $z = 0.37h_m$, and $z = 0.9h_m$. The geostrophically balanced background flow is from south to north. Values of the parameter $\hat{h}$ are indicated inside each panel. Note that the panel aspect ratio (height-to-width) is smaller than the true aspect ratio.

Barotropically forced flow past an elongated ridge leads to vorticity generation along the slopes, culminating in the shedding of vertically coherent vortices into the wake. In section 3, we derive an integral formulation of the vertical vorticity equation that explicitly connects BPT with bottom frictional effects, allowing for a quantification of the quasi-Lagrangian vorticity evolution along barotropic streamlines. We shall demonstrate in section 4 that while the stress does weaken substantially on the slopes as the flow evolves downstream, significant vorticity generation (e.g., Fig. 1) occurs during the early flow encounter with the ridge, as a result of the bottom stress divergence torque (BSDT), a source term in the integrated vorticity equation.

The central role of BSDT raises questions about previous studies that have demonstrated vorticity generation without bottom drag. Among the earliest such studies are the numerical experiments of Smolarkiewicz and Rotunno (1989). In their free-slip simulations of for nonrotating, low-Froude-number flows past topography, a symmetric pair of vertically oriented lee vortices was observed to form in the wake. Using asymptotic arguments, the authors demonstrated that the vertical vorticity was created purely through the tilting of baroclinically generated horizontal vorticity. Since then, lee vortices have been reported in several other studies of nonrotating flows employing zero-stress or free-slip bottom boundary conditions (e.g., Ólafsson and Bougeault 1996; Jagannathan et al. 2019; Puthan et al. 2020). However, to our knowledge there are no studies documenting vorticity generation without bottom drag using ROMS or other realistic ocean models that include the effect of rotation, nor are there any studies making a quantitative comparison between drag and no-drag solutions. These questions will be addressed in section 5, both theoretically and numerically, with a bottom-drag-free ROMS configuration.

2. Model setup

The simulations are performed using ROMS (Shchepetkin and McWilliams 2005), a split-explicit, terrain-following (σ coordinate) ocean model that solves the primitive, hydrostatic equations of motion, with a nonlinear equation of state for seawater (Jackett and McDougall 1995).

We consider a ridge of height h_m and Gaussian half-width a, elongated in the flow direction y. Mathematically the ridge elevation is given by

$$h = h_m e^{-x^2/a^2} \left[\frac{1 + \tanh\left(\frac{y - y_1}{\sigma_y}\right)}{2} \right] \left[\frac{1 + \tanh\left(\frac{y_2 - y}{\sigma_y}\right)}{2} \right], \quad (1)$$

where σ_y represents the extent of the initial encounter region over which the ridge height changes rapidly. One of the motivations for considering an elongated ridge is that it allows for longer downstream development of the cross-slope Ekman dynamics and is thus well suited for studying the departure from one-dimensional and doubly periodic models of slope BBLs and Ekman arrest. The Ekman adjustment problem will be separately considered in a forthcoming study.

In all our simulations, we set $h_m = 400$ m, the half-width $a = 3.5$ km, length $b = y_2 - y_1 = 144$ km, and the encounter length $\sigma_y = 12$ km. Note that these choices imply $b \gg a$ and $\sigma_y = \mathcal{O}(a)$, so that the bathymetry contours are in the shape of a racetrack with a long straight section. The ridge is centered in a computational domain that is 240 km long and 90 km wide.

The simulations have a horizontal resolution of 300 m and 110 σ levels. To resolve BBL dynamics, the ROMS grid is stretched at the bottom so that the vertical resolution ranges from 1.1 m over the flat bottom to 0.9 m at the ridge crest. The turbulent bottom drag is parameterized using a quadratic drag law,

$$\tau_b = \rho_0 C_d \mathbf{u}_b ||\mathbf{u}_b||. \tag{2}$$

In Eq. (2), ρ_0 is a constant reference density, and C_d is the drag constant given by

$$C_d = [\kappa/\log(\Delta z_b/z_{\text{ob}})]^2 \tag{3}$$

where $\kappa = 0.4$ is the von Karman constant, Δz_b is the thickness of the bottommost σ layer and z_{ob} is the roughness length, set to 1 cm. Vertical mixing in the BBL is parameterized using KPP (Large et al. 1994; McWilliams et al. 2009). It is pertinent to note that, in addition to parameterized vertical mixing, both in the BBL and interior, the third-order upwind-biased scheme used for computing the nonlinear advective terms additionally introduces horizontal hyperdiffusive terms (Shchepetkin and McWilliams 2003, 2005).

The solutions are initialized with a uniform barotropic inflow of speed $V_0 = 0.1\,\text{m s}^{-1}$, geostrophically balanced by a zonal gradient in the sea surface elevation, along with a linear vertical profile of potential temperature θ. With the nonlinear equation of state, this produces an approximately uniform background stratification N, permitting the definition of a nondimensional ridge height

$$\hat{h} = \frac{N h_m}{f a}, \tag{4}$$

where f is the Coriolis frequency. Note that $\hat{h}$ may also be interpreted as a slope Burger number (Brink and Lentz 2010; Wenegrat and Thomas 2020). For $\hat{h} \ll 1$, Srinivasan et al. (2019) observed that solutions remained steady and retained essential features of the inviscid quasigeostrophic flow (Schär and Davies 1988; Schär 2002), even with a turbulent bottom drag parameterization. In the same study, values of $\hat{h}$ larger than 1 were found to yield eddying solutions. Here one of our objectives is to understand the process of vertical vorticity generation on the ridge slopes; our primary interest is the eddying regime.

The Coriolis frequency f is fixed at a typical midlatitude value of $7 \times 10^{-5}\,\text{s}^{-1}$ and $\hat{h}$ is varied by changing N alone. The flow variables are held constant at the inflow, with open, radiative conditions (Marchesiello et al. 2001) applied at the other boundaries. We consider four values of $\hat{h}$—1.6, 3.2, 6.4, and 12.8—for which N ranges from $5 \times 10^{-4}\,\text{s}^{-1}$ to $4 \times 10^{-3}\,\text{s}^{-1}$. In this parameter space $\hat{h} > 1$, the dynamics are independent of the water depth H, provided it is larger than the ridge height itself (Srinivasan et al. 2019). Here, H is set to 1000 m. Two sets of solutions are examined—one with, and the other, without bottom drag. All the simulations are run for four months of physical time. Flow variables and momentum diagnostics are output twice daily and temporal averaging is performed over the last two months of the model output so as to exclude the spinup time.

3. Theoretical formulation

a. An integrated vorticity balance

We develop a vertically integrated vorticity formulation to analyze the vorticity balances in our solutions. The central question is, what causes vorticity generation when a current encounters sloping bathymetry. The hitherto overlooked role of the bottom stress divergence torque (BSDT), which appears as one of the boundary terms in this formulation, will be demonstrated in section 4.

The starting point for our analysis are the 2D horizontal momentum equations in vorticity form, supplemented by the continuity equation for mass conservation. In the absence of external forcing, these are

$$\frac{\partial \mathbf{u}}{\partial t} + (\zeta + f)\hat{\mathbf{k}} \times \mathbf{u} + w\frac{\partial \mathbf{u}}{\partial z} = -\nabla_H\left(\frac{p}{\rho_0} + \frac{|\mathbf{u}|^2}{2}\right) + \frac{1}{\rho_0}\frac{\partial \boldsymbol{\tau}}{\partial z}, \tag{5a}$$

$$\nabla_H \cdot \mathbf{u} = -\frac{\partial w}{\partial z}, \tag{5b}$$

where $\mathbf{u}$ is the horizontal velocity vector, ∇_H is the horizontal gradient operator, $\zeta\hat{\mathbf{k}} = \nabla_H \times \mathbf{u}$ is the vertical vorticity, $\partial\boldsymbol{\tau}/\partial z$ is the vertical stress divergence and other symbols have their usual meaning. Note that ROMS also has horizontal hyperviscosity through the third-order upwind biased scheme, but this is a negligible term in the vorticity balances for our simulations.

After taking the horizontal curl of Eq. (5a), using standard vector calculus identities and dotting with $\hat{\mathbf{k}}$, we have the vorticity equation

$$\underbrace{\frac{\partial \zeta}{\partial t} + \mathbf{u}\cdot\nabla_H\zeta + w\frac{\partial \zeta}{\partial z}}_{\frac{D\zeta}{Dt}} = \underbrace{(\zeta + f)\frac{\partial w}{\partial z}}_{\text{vortex stretching}} \underbrace{- -\left(\nabla_H w \times \frac{\partial \mathbf{u}}{\partial z}\right)\cdot\hat{\mathbf{k}}}_{\text{vortex tilting}}$$
$$- \beta v + \underbrace{\hat{\mathbf{k}}\cdot\nabla_H \times \left(\frac{1}{\rho_0}\frac{\partial \boldsymbol{\tau}}{\partial z}\right)}_{\text{stress divergence curl}}. \tag{6}$$

As f is constant in our simulations, we neglect the β effect. To obtain the integrated vorticity equation, vertically integrate Eq. (6) from $z = -H + h(x, y)$ to $z = \eta$, where H is the constant water depth away from the topography and η is the sea surface elevation,

$$\int_{-H+h}^{\eta} \frac{D\zeta}{Dt}\,dz = \int_{-H+h}^{\eta} (\zeta + f)\frac{\partial w}{\partial z}\,dz - \int_{-H+h}^{\eta}\left(\nabla_H w \times \frac{\partial \mathbf{u}}{\partial z}\right)\cdot\hat{\mathbf{k}}\,dz + \int_{-H+h}^{\eta}\hat{\mathbf{k}}\cdot\nabla_H \times \left(\frac{1}{\rho_0}\frac{\partial \boldsymbol{\tau}}{\partial z}\right)dz. \tag{7}$$

Further, in the absence of a surface wind stress and taking the curl outside the integral, the last term in Eq. (7) can be rewritten using Leibniz's rule as

$$\int_{-H+h}^{\eta} \hat{\mathbf{k}} \cdot \nabla_H \times \left(\frac{1}{\rho_0}\frac{\partial \boldsymbol{\tau}}{\partial z}\right) = -\hat{\mathbf{k}} \cdot \left(\frac{1}{\rho_0}\nabla_H \times \boldsymbol{\tau}_b\right) - \hat{\mathbf{k}} \cdot \left(\frac{1}{\rho_0}\frac{\partial \boldsymbol{\tau}}{\partial z}\bigg|_b \times \nabla_H h\right) \tag{8}$$

where the subscript b denotes "bottom." Note that the first term on the RHS is the familiar bottom stress curl (BSC). The second term $-(\{\partial \boldsymbol{\tau}/\partial z\}|_b/\rho_0) \times \nabla_H h$ appears as a result of interchanging the curl and integral operators. We refer to this as the bottom stress divergence torque (BSDT). It is the twisting force produced due to the vertical divergence of stress in the direction orthogonal to the topographic gradient $\nabla_H h$. Equation (7) now becomes

$$\int_{-H+h}^{\eta} \frac{D\zeta}{Dt} dz = \underbrace{\int_{-H+h}^{\eta} (\zeta + f)\frac{\partial w}{\partial z} dz}_{\text{VS}} \underbrace{- \int_{-H+h}^{\eta} \left(\nabla_H w \times \frac{\partial \mathbf{u}}{\partial z}\right) \cdot \hat{\mathbf{k}}\, dz}_{\text{VT}} \underbrace{-\hat{\mathbf{k}} \cdot \left(\frac{1}{\rho_0}\nabla_H \times \boldsymbol{\tau}_b\right)}_{\text{BSC}} \underbrace{-\hat{\mathbf{k}} \cdot \left(\frac{1}{\rho_0}\frac{\partial \boldsymbol{\tau}}{\partial z}\bigg|_b \times \nabla_H h\right)}_{\text{BSDT}}. \tag{9}$$

Here the acronyms VS, VT, and BSC, respectively, stand for vortex stretching, vortex tilting, and bottom stress curl.

To see how the bottom pressure torque (BPT), defined as

$$\text{BPT} = -\nabla_H \left(\frac{p_b}{\rho_0}\right) \times \nabla_H h, \tag{10}$$

is connected to BSDT, we apply the horizontal momentum balance Eq. (5a) at the bottom and take the cross product with $\nabla_H h$. This yields the relation

$$\frac{1}{\rho_0}\frac{\partial \boldsymbol{\tau}}{\partial z}\bigg|_b \times \nabla_H h = \frac{\partial \mathbf{u}_b}{\partial t} \times \nabla_H h + \nabla_H \left(\frac{p_b}{\rho_0} + \frac{|\mathbf{u}_b|^2}{2}\right) \times \nabla_H h - (\zeta_b + f)u_b \cdot \nabla_H h \hat{\mathbf{k}} + w_b \frac{\partial \mathbf{u}_b}{\partial z} \times \nabla_H h. \tag{11}$$

An interesting limit is that of a no-slip bottom boundary. Equation (11) then reduces to

$$\frac{1}{\rho_0}\frac{\partial \boldsymbol{\tau}}{\partial z}\bigg|_b \times \nabla_H h = \nabla_H \left(\frac{p_b}{\rho_0}\right) \times \nabla_H h, \tag{12}$$

meaning that BSDT and BPT balance exactly. Note, however, that Eq. (11) and not Eq. (12) is the appropriate balance in discretized ocean models such as ROMS which employ a turbulent bottom stress parameterization, with Monin–Obukhov similarity theory assumed to apply within the bottom grid cell.

Equations (11) and (12) underscore the direct relationship between BPT and BSDT. As we will further see in section 4d, this resolves the apparently contradictory explanations for vorticity generation provided here and in previous studies such as Molemaker et al. (2015) and Gula et al. (2015).

b. *Quasi-Lagrangian analysis*

We now develop a quasi-Lagrangian technique for analyzing the integrated vorticity equation, Eq. (9). We call it quasi-Lagrangian as opposed to Lagrangian to emphasize the fact that we will be tracking the evolution of source terms on mean barotropic streamlines and not individual particle trajectories.

Consider again, the integrated vorticity equation, Eq. (9). To simplify the algebra, we neglect temporal fluctuations of the sea surface elevation η. Now, denoting time averages by $\overline{(\cdot)}$ and combined depth and time averages by $\langle\ \rangle$, we can write the time-averaged equation (9) as

$$\int_{-H+h}^{\eta} \nabla_H \cdot (\overline{\mathbf{u}\zeta})\, dz + \int_{-H+h}^{\eta} \frac{\partial (\overline{w\zeta})}{\partial z} = \int_{-H+h}^{\eta} \overline{(\zeta + f)\frac{\partial w}{\partial z}} dz - \int_{-H+h}^{\eta} \overline{\left(\nabla_H w \times \frac{\partial \mathbf{u}}{\partial z}\right)} \cdot \hat{\mathbf{k}}\, dz - \hat{\mathbf{k}} \cdot \frac{1}{\rho_0}\nabla_H \times \overline{\boldsymbol{\tau}_b} - \hat{\mathbf{k}} \cdot \frac{1}{\rho_0}\frac{\overline{\partial \boldsymbol{\tau}}}{\partial z}\bigg|_b \times \nabla_H h. \tag{13}$$

Note that the time derivative term in Eq. (13) has been dropped. Formally, this approximation is valid in a statistically steady state, and in the limit of a long time average.

Using Leibniz's rule to interchange the integral and divergence operators on the LHS of the above equation and invoking boundary conditions of free surface at the top and no-normal flow at the bottom, $\mathbf{u}_s \cdot \nabla \eta = w_s$ and $\mathbf{u}_b \cdot \nabla h = w_b$, respectively, after cancellation of the boundary terms we have

$$\nabla_H \cdot [\langle \mathbf{u}\zeta \rangle D] = \underbrace{\int_{-H+h}^{\eta} \overline{(\zeta + f)\frac{\partial w}{\partial z}} dz}_{\text{VS}} \underbrace{- \int_{-H+h}^{\eta} \overline{\left(\nabla_H w \times \frac{\partial \mathbf{u}}{\partial z}\right)} \cdot \hat{\mathbf{k}}\, dz}_{\text{VT}} \underbrace{-\hat{\mathbf{k}} \cdot \frac{1}{\rho_0}\nabla_H \times \overline{\boldsymbol{\tau}_b}}_{\text{BSC}} \underbrace{-\hat{\mathbf{k}} \cdot \frac{1}{\rho_0}\frac{\overline{\partial \boldsymbol{\tau}}}{\partial z}\bigg|_b \times \nabla_H h}_{\text{BSDT}}, \tag{14}$$

where $D = (H - h + \eta)$ is the local water column depth.

We now decompose the advection term into mean and eddy components, where the eddy component here represents fluctuations from the combined depth and time average.

$$\overline{\mathbf{U}} \cdot \nabla_H \langle \zeta \rangle + \langle \zeta \rangle \cancel{\nabla_H \cdot \overline{\mathbf{U}}}^{0} = \int_{-H+h}^{\eta} \overline{(\zeta + f)\frac{\partial w}{\partial z}} dz - \int_{-H+h}^{\eta} \overline{\left(\nabla_H w \times \frac{\partial \mathbf{u}}{\partial z}\right)} \cdot \hat{\mathbf{k}}\, dz - \hat{\mathbf{k}} \cdot \frac{1}{\rho_0}\nabla_H \times \overline{\boldsymbol{\tau}_b} - \hat{\mathbf{k}} \cdot \frac{1}{\rho_0}\frac{\overline{\partial \boldsymbol{\tau}}}{\partial z}\bigg|_b \times \nabla_H h - \nabla_H \cdot [\langle \mathbf{u}\zeta' \rangle D], \tag{15}$$

where

$$\overline{\mathbf{U}} = \int_{-H+h}^{\eta} \overline{\mathbf{u}}\, dz \tag{16}$$

is the time-mean barotropic transport. Equation (15) can be written in characteristic form as

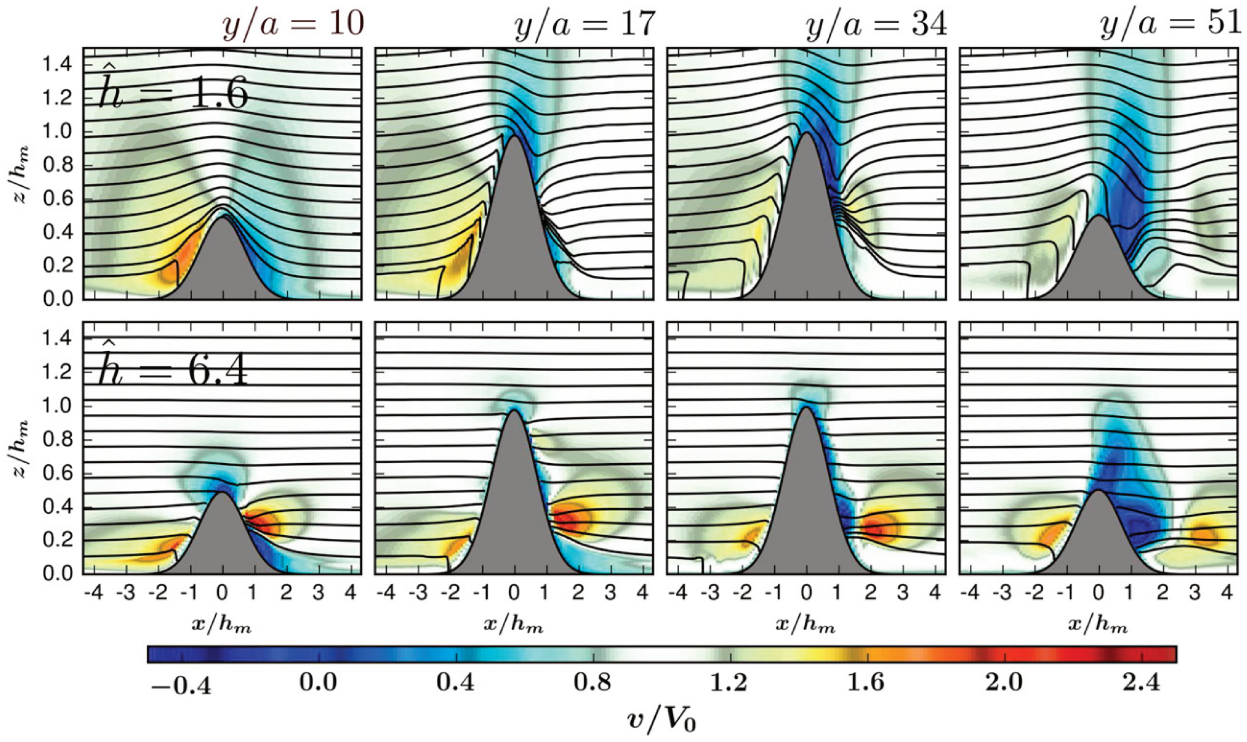

FIG. 2. Vertical sections of normalized, time-mean along-slope velocity v/V_0 overlain by isopycnals at successive downstream locations: (top) $\hat{h} = 1.6$ and (bottom) $\hat{h} = 6.4$.

$$\overline{|\mathbf{U}|}\frac{\partial\langle\zeta\rangle}{\partial s} = \int_{-H+h}^{\eta}\overline{(\zeta+f)\frac{\partial w}{\partial z}}\,dz - \int_{-H+h}^{\eta}\left(\overline{\nabla_H w\times\frac{\partial\mathbf{u}}{\partial z}}\right)\cdot\hat{\mathbf{k}}\,dz - \hat{\mathbf{k}}\cdot\frac{1}{\rho_0}\nabla_H\times\overline{\tau_b} - \hat{\mathbf{k}}\cdot\frac{1}{\rho_0}\left.\frac{\overline{\partial\tau}}{\partial z}\right|_b\times\nabla_H h - \nabla_H\cdot[\langle u'\zeta'\rangle D], \tag{17}$$

where s now denotes the distance along the characteristics, i.e., barotropic streamlines of the flow. Equation (17) can then be integrated to determine the evolution of the depth averaged vorticity $\langle\zeta\rangle$ and hence also the vertically integrated vorticity $\overline{\omega} = \langle\zeta\rangle D$ along the barotropic streamlines as

$$\overline{\omega}(s) = \langle\zeta\rangle D = D\int_0^{s(x,y)}\frac{1}{\overline{|\mathbf{U}|}}\left[\underbrace{\int_{-H+h}^{\eta}\left[\overline{(\zeta+f)\frac{\partial w}{\partial z}}\right]dz}_{\text{VS}} - \underbrace{\int_{-H+h}^{\eta}\left(\overline{\nabla_H w\times\frac{\partial\mathbf{u}}{\partial z}}\right)\cdot\hat{\mathbf{k}}\,dz}_{\text{VT}}\underbrace{-\hat{\mathbf{k}}\cdot\frac{1}{\rho_0}\nabla_H\times\overline{\tau_b}}_{\text{BSC}} \underbrace{-\hat{\mathbf{k}}\cdot\frac{1}{\rho_0}\left.\frac{\overline{\partial\tau}}{\partial z}\right|_b}_{\text{BSDT}} \underbrace{-\nabla_H\cdot[\langle\mathbf{u}'\zeta'\rangle D]}_{\text{eddy advection}}\right]ds. \tag{18}$$

In section 4b we will use Eq. (18) to identify which terms are responsible for vorticity generation as a current encounters topography and advects along its slopes.

4. Frictional vorticity generation

a. Vertical structure of the solutions

We briefly discuss the vertical flow structure in our solutions before proceeding to examine the balances in the integrated vorticity equation. In the remainder of the paper, we refer to the side where uphill is to the left (right) of the along-slope flow as the cyclonic (anticyclonic) side, consistent with a Northern Hemisphere orientation.

Figure 2 displays vertical sections of the mean flow structure at successive downstream locations starting from the encounter region, for $\hat{h} = 1.6$ and 6.4. For all $\hat{h}$, there is an asymmetry in the along-slope velocity between the cyclonic and anticyclonic sides, arising due to the effect of background rotation. As the flow encounters the ridge, isopycnals deflect upslope (downslope) on the cyclonic (anticyclonic) side in response to Ekman induced upwelling (downwelling) (e.g., Garrett et al. 1993; Brink and Lentz 2010).

At $\hat{h} = 1.6$, we note the presence of a circulation around the ridge, characterized by an accelerated flow along the straight section of the ridge on the anticyclonic side that is compensated by deceleration above the cyclonic slope. This is

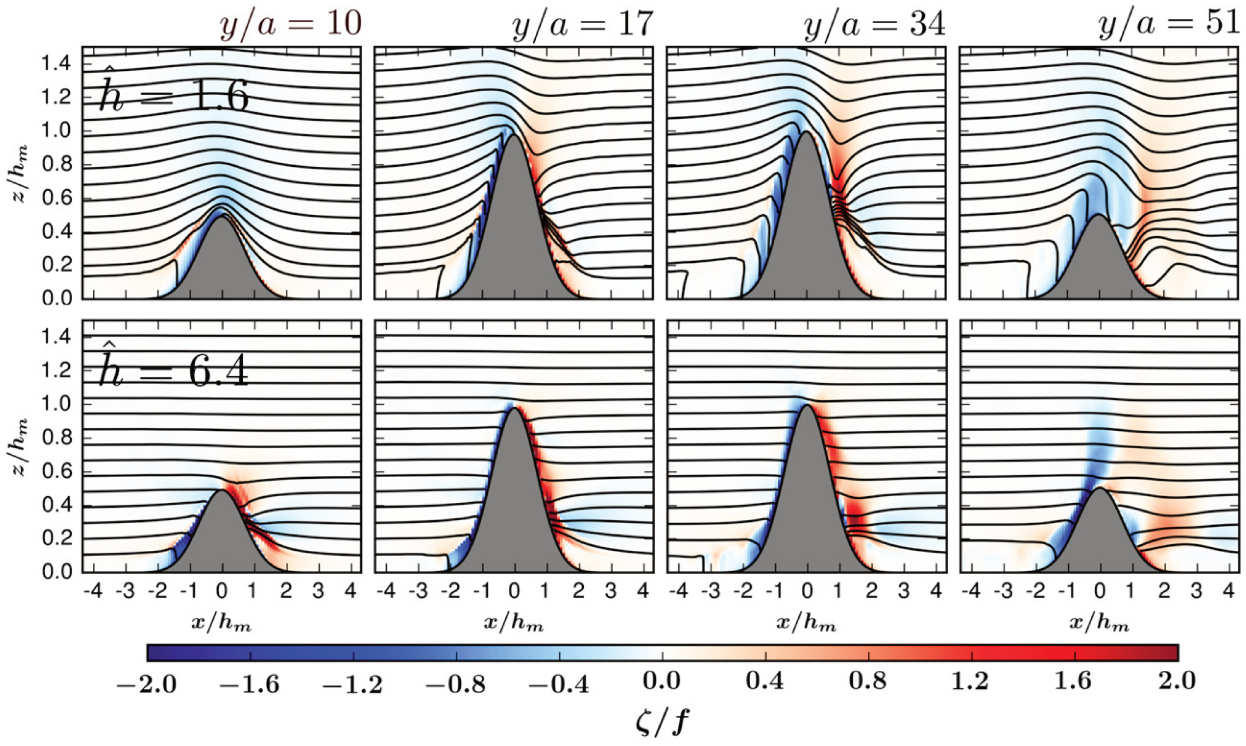

FIG. 3. Vertical sections of normalized, time-mean vertical vorticity ζ/f overlain by isopycnals at successive downstream locations: (top) $\hat{h} = 1.6$ and (bottom) $\hat{h} = 6.4$.

reminiscent of quasigeostrophic dynamics (e.g., Fig. 2 of Srinivasan et al. 2019), in which squashing of vortex tubes leads to the formation of an anticyclone on top of the obstacle. While quasigeostrophic solutions for most obstacle shapes are formally valid only up to some critical value of $\hat{h} < 1$ (Schär 2002), residual circulations can persist for higher $\hat{h}$, as the $\hat{h} = 1.6$ case in Fig. 2 shows. At $\hat{h} = 6.4$, the circulation becomes much weaker and the vertical shear on the cyclonic side increases, as evidenced by the emergence of a baroclinic jet above the upslope Ekman flow. The concomitant loss of vertical coherence in the vorticity structure is visible in Fig. 3 below.

Figure 3 depicts the along-slope evolution of vorticity. The topographic interaction produces strong vertical vorticity [$|\zeta|/f = \mathcal{O}(1)$] adjacent to the slope on either side of the ridge. As the flow evolves downstream (y/a = 17, 34), vertical alignment of the vorticity occurs and a distinct columnar structure emerges. This is more pronounced on the cyclonic side and at $\hat{h} = 1.6$ and 3.4 (not shown). The genesis of topographically generated SCVs is a result of the eventual separation of these columnar vortices from the slopes. Note that the vortices become increasingly decorrelated vertically at $\hat{h} = 6.4$. As we will see, after the separation of the current from the slopes ($y/a = 51$), advection of eddy vorticity, encapsulated by the term EA in Eq. (9), causes the time-mean vorticity to decrease.

b. The role of the BBL in topographic vorticity generation

The advantage of the integrated vorticity formulation in Eq. (9) is that BSC and BSDT expressly illuminate the role of the bottom stress in the vorticity generation process. These terms represent nonconservative, viscous torques. By contrast, BPT, as it appears in the barotropic vorticity equation, can be difficult to interpret in ocean models, which rely on turbulent BBL parameterizations rather than an explicitly enforced no-slip condition.

The one-dimensional theory of boundary currents (MacCready and Rhines 1991) predicts a slow temporal evolution toward bottom stress collapse and hence boundary layer shutdown on slopes. However, on realistic topography, Ekman adjustment is a primarily downstream rather than temporally evolving process. Moreover, flow separation and secondary instabilities will alter the leading-order cross-slope momentum balance and a departure from the steady state one-dimensional prediction is to be expected. Indeed, while the bottom stress (Fig. 4) on the higher reaches of the ridge exhibits substantial weakening downstream with increasing $\hat{h}$, it is far from a state of collapse at the lower slopes. BBL mediated vorticity generation occurs during the early Ekman adjustment process over the encounter region, as exemplified in Fig. 3. This is consistent with findings in Benthuysen and Thomas (2012) and Ruan et al. (2019) that the Ekman adjustment process is itself a means of generating vorticity.

For finite N, the BBL height h_{bbl} on a flat bottom follows the empirical scaling $h_{\mathrm{bbl}} \sim u^*/\sqrt{Nf}$ (McWilliams et al. 2009), where $u^* = \sqrt{\tau_b/\rho_0}$ is the friction velocity. In Fig. 5 we show the time-mean h_{bbl} as a function of the cross-slope coordinate x at two downstream locations, one in the encounter region and the other roughly halfway along the ridge. The BBL height h_{bbl} as defined here is the depth over which active shear-driven

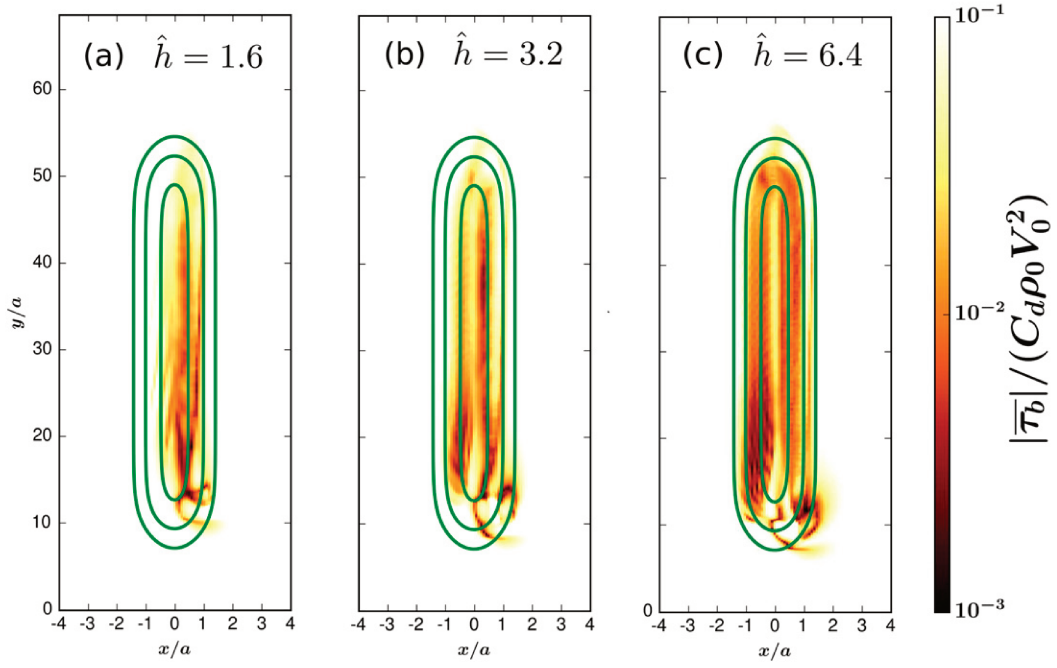

FIG. 4. Normalized, time-averaged boundary stress. Values of the parameter $\hat{h}$ are indicated inside each panel.

entrainment and mixing occur. It is computed in ROMS using KPP, which parameterizes the effects of stratified Ekman layer turbulence. Note that h_{bbl} is different from the mixed layer depth which is the quantity of interest in the Ekman adjustment problem. The dimensional h_{bbl} have been normalized by $3u^*/\sqrt{Nf}$ (Srinivasan et al. 2019), where u^* is taken as the average value of the friction velocity over the flat bottom, away from the ridge. For all $\hat{h}$, h_{bbl} in the encounter region ($y/a = 10$) is larger on the anticyclonic side—a consequence of the alongslope flow being faster there. Downwelling on the anticyclonic side transports heavier fluid under lighter fluid, making the flow convectively unstable. Parameterized vertical mixing in ROMS then leads to the formation of a bottom mixed layer which continues to deepen moving downstream.

The dominant tendency terms in the vertical vorticity equation, Eq. (6) are displayed in Fig. 6. The stress divergence curl within the BBL initiates vorticity generation during the early encounter, with advective processes being a secondary source in the flow interior. Vortex stretching occurs in response to Ekman upwelling and downwelling in the BBL. Further aloft, the oscillatory structure of VS + VT is due to vertical internal wave modes that are launched when the flow encounters the ridge. Assuming rotational effects are small, the vertical wavelength of these waves is proportional to V_0/N (e.g., Baines 1998). Hence for fixed V_0, it scales inversely with $\hat{h}$. Finally, vertical vorticity is also created through tilting of horizontally oriented vortex tubes. In section 5, we will further illustrate using simulations and asymptotic arguments how stretching and tilting effects can generate vorticity even in the absence of bottom drag.

With a view to quantifying precisely how drag against the ocean bottom injects vertical vorticity into the flow, we now

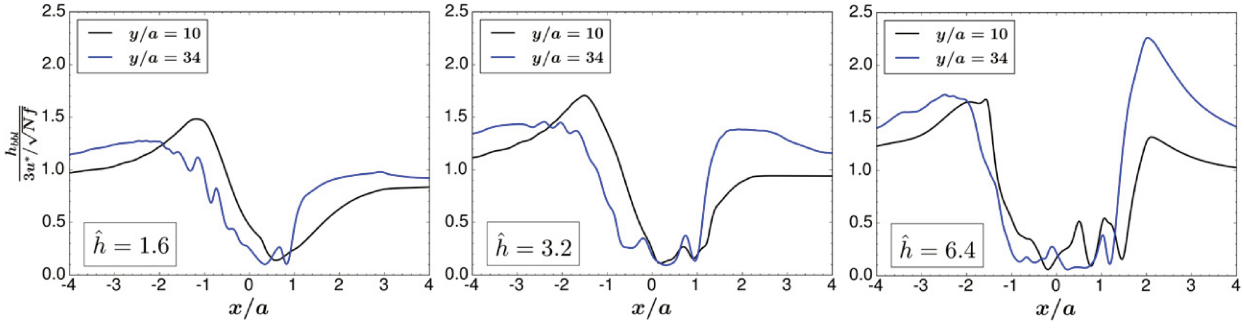

FIG. 5. The time-mean BBL height h_{bbl} normalized by $3u^*/\sqrt{Nf}$ at two different locations—one in the encounter region ($y/a = 10$) and the other further downstream ($y/a = 34$). Values of the parameter $\hat{h}$ are indicated inside each panel. Note that u^* here is taken to be the average friction velocity over the flat bottom, away from the ridge, for the respective $\hat{h}$ cases. The dimensional h_{bbl} are smaller for larger $\hat{h}$.

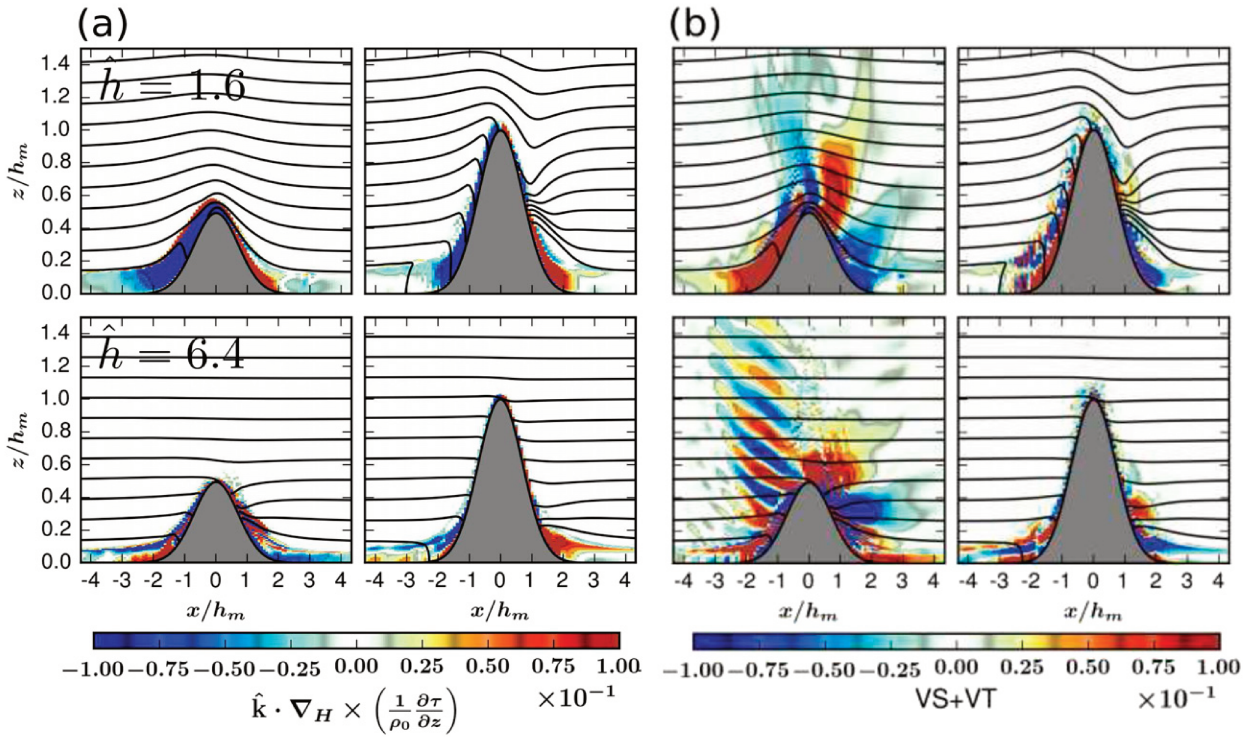

FIG. 6. Time-averaged tendency terms in the 3D vertical vorticity equation, Eq. (6), normalized by fV_0a^{-1} and overlain by flow isopycnals for (top) $\hat{h} = 1.6$ and (bottom) $\hat{h} = 6.4$, indicated inside the leftmost panel. (a) Stress divergence curl and (b) VS + VT, the sum of vortex stretching and tilting terms in Eq. (6). The subpanel columns in (a) and (b) depict the following vertical sections: (left) at encounter region $y/a = 10$ and (right) averaged across the straight section of the ridge.

examine the integrated vorticity balances in our solutions. Using the momentum diagnostics directly from ROMS, the various source terms in the integrated vorticity equation, Eq. (9) are computed to the level of ROMS accuracy. Snapshots and time averages of the vertically integrated vorticity are displayed in Figs. 1 and 7 respectively. Also displayed in Fig. 7 are the streamlines of the mean barotropic transport. The rotation-induced asymmetry is clearly visible in the streamline patterns.

In a Lagrangian reference frame, water columns on the cyclonic (anticyclonic) side acquire positive (negative) vorticity as they advect downstream along mean transport streamlines. As the flow separates from the slopes, vorticity generation is followed by rapid merger events where smaller like-signed vortices roll up to form larger ones (Srinivasan et al. (2019)) that eventually separate further downstream as submesoscale coherent vortices. The prominent small-scale structures seen on the anticyclonic side are manifestations of hybrid centrifugal/symmetric instability of the flow (e.g., Wenegrat and Thomas 2020). This aspect of the solutions will be further explored in a follow up study.

In Fig. 8 we plot each of the tendency terms of the integrated vorticity equation as they appear on the RHS of Eq. (9). Interestingly, the BSC is of minor importance, and further, is a sink rather than a source of vorticity on both sides of the ridge, regardless of the value of $\hat{h}$. Instead, much of the vorticity injection occurs around the early encounter region through the action of BSDT. On the cyclonic side, the net effect of vortex stretching and tilting (denoted VSVT) as a sink of vorticity is evident: however, Fig. 8 is somewhat inconclusive with respect to its role on the anticyclonic side.

To gain further insight into the interplay of BSDT and VSVT as a water column advects along a topographic slope, we take recourse to the quasi-Lagrangian technique described in section 3b. Partial cumulative integrals of the source terms of $\overline{\omega}$ [as they appear on the RHS of Eq. (18)] are computed along mean transport streamlines (depicted in Fig. 7). The streamlines are chosen to pass through the hotspots of BSDT and VSVT in the encounter region (Fig. 8) and advect downstream along the straight section of the ridge. Averaging over several such streamlines, as depicted in Fig. 7, separately on each of the cyclonic and anticyclonic sides, Fig. 9 shows that along the cyclonic slope, BSDT continuously injects vorticity into the flow, while VSVT acts to deplete it. The eddy advection term EA represents conversion from mean to eddy vorticity and vice versa. It acts as a source term on the slopes and a sink after flow separation.

On the anticyclonic side, BSDT is again the dominant generation term. A notable observation is that, for the $\hat{h} = 6.4$ case, there is a reversal in tendencies immediately past the encounter region ($y/a \approx 16$) where VSVT and BSDT switch signs. A similar reversal is seen for $\hat{h} = 12.8$ (not shown). Nevertheless, there is no net generation of vorticity after the reversal, much of it having already occurred during the early encounter through BSDT. We have checked that while BSDT continues to act strictly as a source term along certain individual

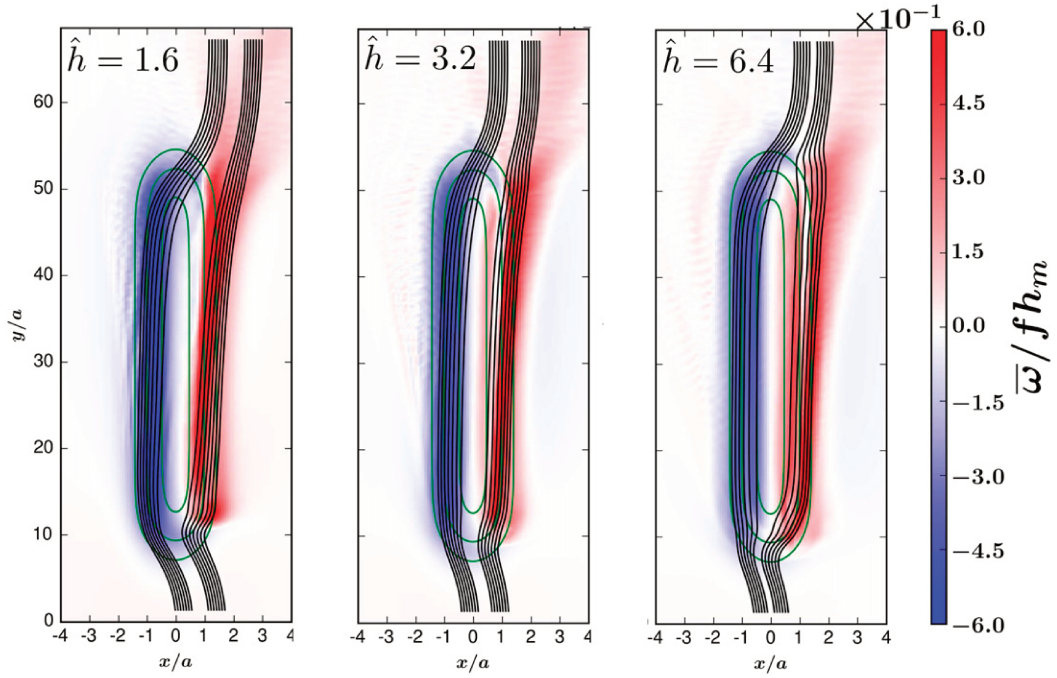

FIG. 7. Time averages of vertically integrated vorticity, normalized by fh_m for the ridge solutions. The black and green contour lines are, respectively, streamlines of the barotropic transport $\mathbf{U}$ and bathymetry contours at $z = 0.14h_m$, $z = 0.37h_m$, and $z = 0.9h_m$. Values of the parameter $\hat{h}$ are indicated inside each panel.

streamlines for these solutions, in a streamline-averaged sense, it nonetheless has the tendency of a sink along the straight section of the ridge. The sign reversal of BSDT implies a negative bottom stress divergence. A possible explanation for this is that it occurs due to the near collapse of bottom stress on the upper reaches of the straight section past the southern edge of the ridge (Fig. 4c). Consequently, in an average sense, parameterized vertical mixing of the convectively unstable downwelling flow dominates bottom stress-driven mixing there, resulting in a positive BSDT. Finally, we remark that the budget for the integrated vorticity in Eq. (18) is closed to within 5% on both the cyclonic and anticyclonic sides.

Along the straight section of the ridge and prior to flow separation, the mean value of the integrated vorticity remains nearly constant. This might be expected, for example, from the geometric argument of Molemaker et al. (2015) according to which the vertical vorticity in the BBL is given by $\overline{\zeta} \approx -\theta \partial \overline{v}/\partial z$, where $|\theta| \ll 1$ is the slope, so that integrating over the BBL yields $\overline{\omega} \approx -\theta V_0$. The nearly constant value of $\overline{\omega}$ along the straight section may also be interpreted as being reflective of Ekman balance, with vortex tilting effects balancing frictional torques (Wenegrat and Thomas 2017).

c. A heuristic explanation for BSC and BSDT patterns

Consider our geometry with a ridge of height $h(x, y)$ and an inflow V_0 directed northward. Assume, heuristically, that the horizontal circulation around the ridge is weak (i.e., $\hat{h} > 1$) and that the main effect of the ridge is to split the flow such that $v(x, y)$ is accelerated on the flanks of the ridge and decelerated over the ridge top, with some broadscale return to the inflow V_0 in the x far field.

The bottom stress and its vertical derivative can be approximated as

$$\tau_b \approx C_d v_b^2 \hat{\mathbf{j}}, \tag{19a}$$

$$\left.\frac{\partial \tau}{\partial z}\right|_b \approx -\frac{C_d v_b^2}{h_{\text{bbl}}}. \tag{19b}$$

The second relation assumes a uniform decrease of the stress over the boundary layer depth. Then we have the following approximations for BSC and BSDT,

$$\text{BSC} = -\hat{\mathbf{k}} \cdot \nabla_H \times \tau_b \approx -C_d v_b \frac{\partial v_b}{\partial x}, \tag{20a}$$

$$\text{BSDT} = -\hat{\mathbf{k}} \cdot \left(\left.\frac{\partial \tau}{\partial z}\right|_b \times \nabla_H h \right) \approx -\frac{C_d v_b^2}{h_{\text{bbl}}} \frac{\partial h}{\partial x}. \tag{20b}$$

For BSC, the left side of the ridge is positive and the right side is negative because of the sign of $\partial v_b/\partial x$; thus, it is opposite to the sense of the vorticity generation. For BSDT, the signs are the opposite due to the opposite sign of $\partial h/\partial x$ on the two sides; thus, this is a generation term. These heuristic predictions are broadly consistent with what we see in our solutions (Fig. 8).

A scale estimate of the ratio of the magnitudes of the two terms is

$$\frac{\text{BSC}}{\text{BSDT}} \sim \frac{\delta v_b}{v_b} \frac{h_{\text{bbl}}}{\delta h}, \tag{21}$$

where δ indicates the size of the changes over the ridge. Further assuming that $\delta v_b \approx v_b$, Eq. (21) then implies that BSC is small relative to BSDT in our solutions simply because h_{bbl} is smaller than h.

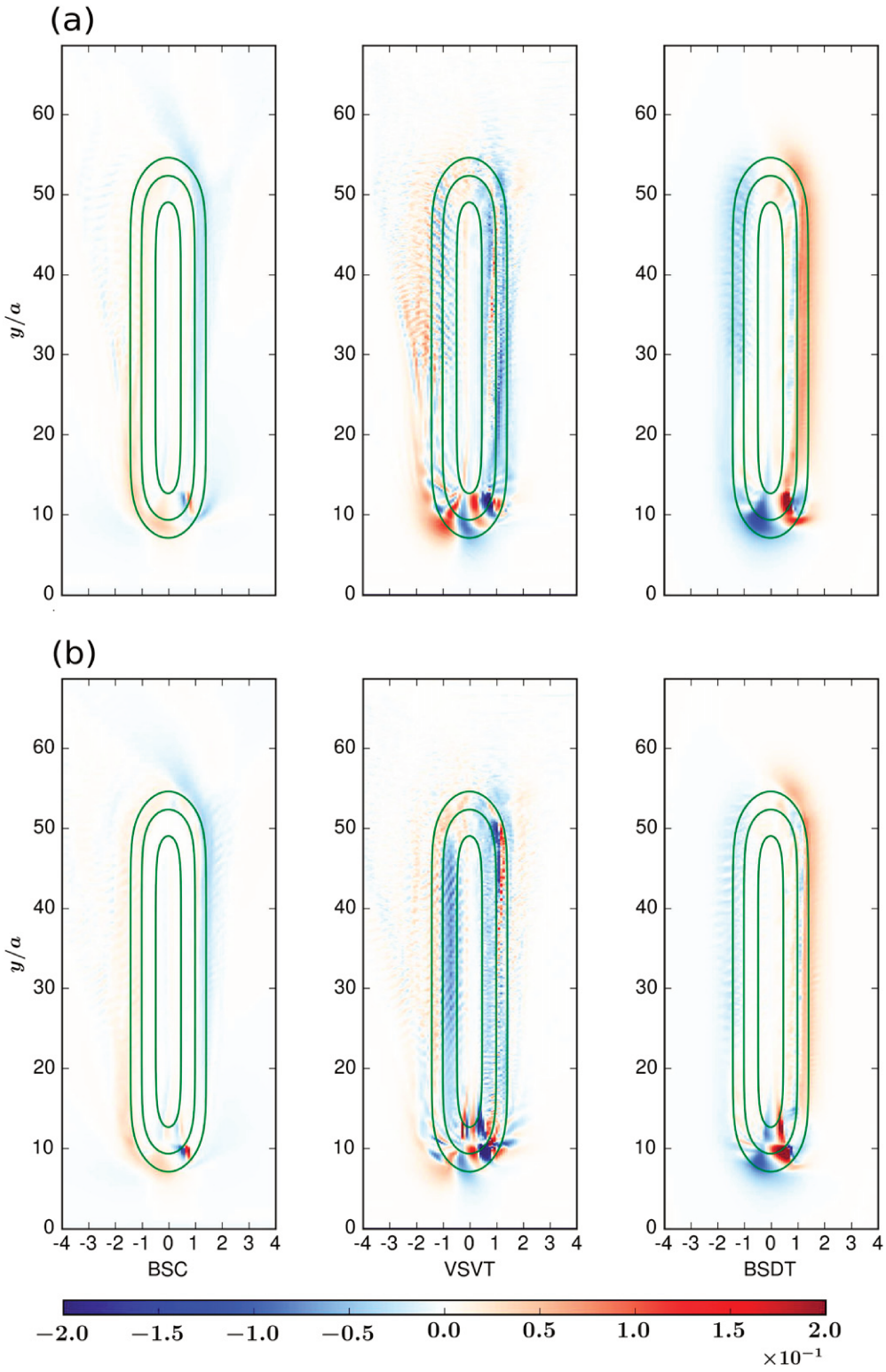

FIG. 8. Time-averaged generation terms on the RHS of the integrated vorticity equation, Eq. (9). VSVT is the sum of the vortex stretching (VS) and tilting (VT) terms. Each term has been normalized by $fh_mV_0a^{-1}$: (a) $\hat{h} = 3.2$ and (b) $\hat{h} = 6.4$.

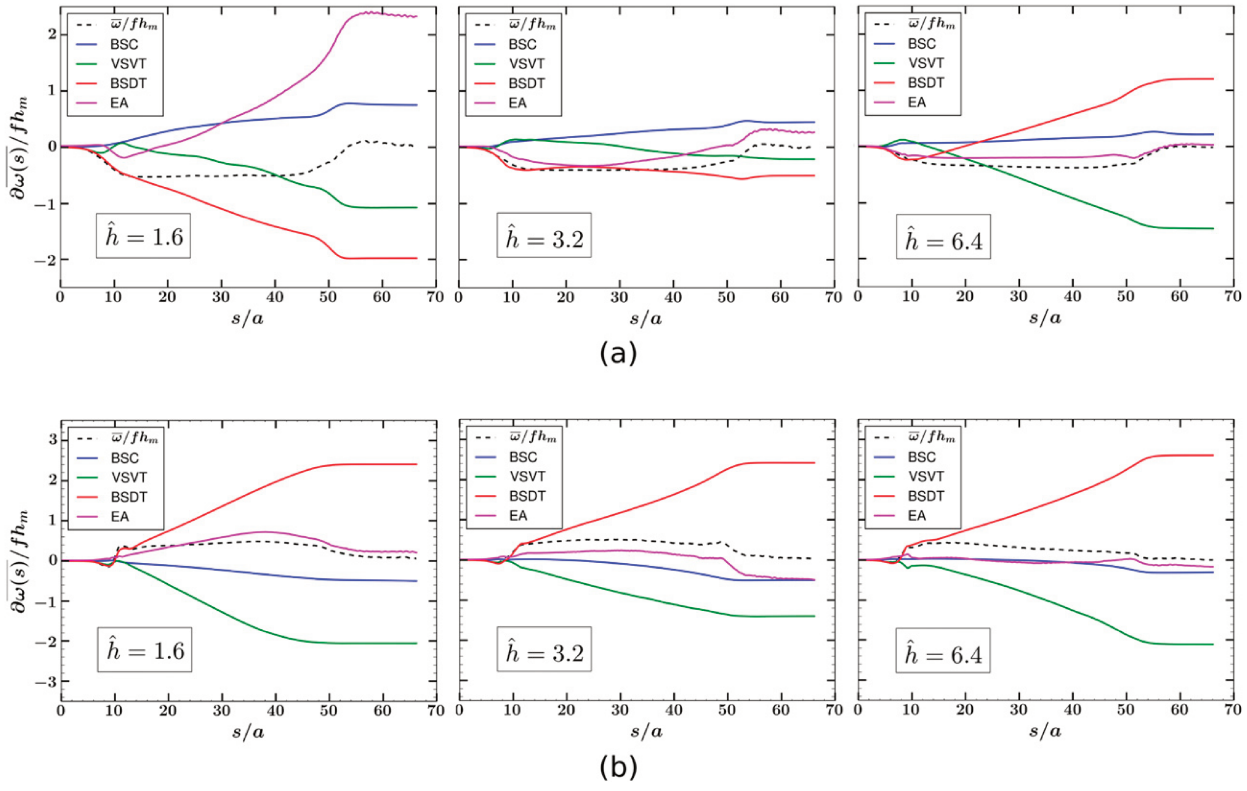

FIG. 9. Partial cumulative integrations of source terms on the RHS of Eq. (18) to $\overline{\omega}$ averaged separately on each of the cyclonic and anticyclonic sides across the streamlines depicted in Fig. 7. BSDT is the bottom stress divergence torque, VSVT denotes the net sum of vortex stretching and tilting terms, and EA is the eddy advection; a is the ridge half-width and s/a is the normalized distance along the streamline. Values of the parameter $\hat{h}$ are indicated inside each panel: (a) anticyclonic side and (b) cyclonic side.

d. The connection between BSDT and BPT

An alternate way to formulate the vorticity balance is by taking the curl of the vertically integrated horizontal momentum equations, Eq. (5a). This yields the so-called barotropic vorticity equation (see, e.g., Hughes and De Cuevas 2001; Gula et al. 2015),

$$\frac{\partial \Omega}{\partial t} = \underbrace{-\hat{\mathbf{k}} \cdot \left(\frac{1}{\rho_0} \nabla_H p_b \times \nabla_H h\right)}_{\text{BPT}} \underbrace{-\hat{\mathbf{k}} \cdot \left(\frac{1}{\rho_0} \nabla_H \times \tau_b\right)}_{\text{BSC}} + \underbrace{A_\Sigma}_{\text{NL terms}}, \tag{22}$$

where, borrowing from the notation in Gula et al. (2015), A_Σ encapsulates all the nonlinear terms and

$$\Omega = \nabla_H \times \mathbf{U} \tag{23}$$

is referred to as the barotropic vorticity. It is related to the vertically integrated vorticity ω through the bottom horizontal velocity as

$$\Omega = \underbrace{\int_{-H+h}^{\eta} \zeta \, dz}_{\omega} + \mathbf{u}_b \times \nabla_H h. \tag{24}$$

Notice that in the no-slip limit, barotropic and vertically integrated vorticity are exactly identical. However, in regional ocean models with a quadratic bottom drag parameterization and a well-resolved BBL, one would instead expect that these are *almost* identical, which is what we find in our simulations.

Recall from Eq. (11) that BPT can be written as the sum of BSDT and nonlinear bottom stretching, tilting and advective contributions. Further, the term A_Σ in Eq. (22) has embedded within it the cumulative effects of nonlinear vortex stretching and tilting in the interior. This implies that, in general, BPT and A_Σ are not necessarily mutually independent with respect to the processes they represent. A comparison of Figs. 10b and 10c, which depicts the time-mean BPT distribution over the ridge, with Fig. 8 reveals the similarity in the patterns of BPT and BSDT. However, the difference of BPT and BSDT, plotted in Figs. 10d–f shows that BPT additionally has a smaller inviscid part to it. The implication is that, when the turbulent BBL is well resolved, the dominant dynamical role of BPT is as a frictional torque, with a smaller "flow turning" component that steers the current around the topography. We shall see in section 5 that the interpretation of BPT changes completely when bottom drag is "turned off" or as may be the case, the BBL resolution is inadequate.

5. Vorticity generation without bottom drag

a. The role of vortex stretching and tilting

We saw in section 4b that, for large $\hat{h}$, the diminishing bottom stress on the anticyclonic side (Fig. 4) causes a reversal of

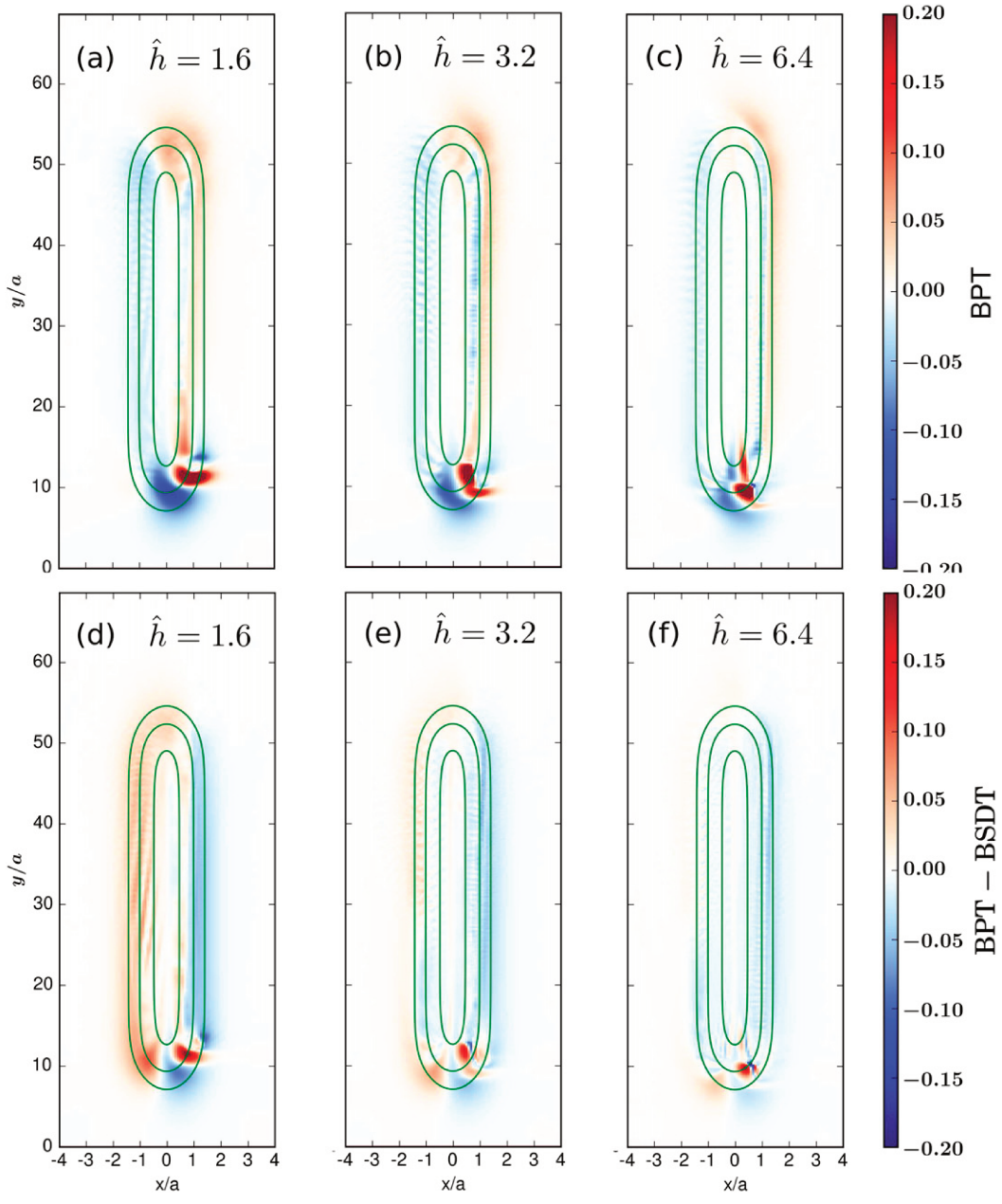

FIG. 10. (top) Bottom pressure torque (BPT), defined in Eq. (10) and (bottom) difference of BPT and BSDT [defined in Eq. (9)], both time-averaged and normalized by $fh_mV_0a^{-1}$. Values of the parameter $\hat{h}$ are indicated inside each panel.

tendencies along the straight section of the ridge whereby VSVT becomes a source and BSDT a sink of mean vorticity in the evolution Eq. (9) (see also Fig. 9). Nevertheless, we saw that this reversal does not lead to net generation of vorticity by VSVT. To explore the possibility of vorticity generation purely by vortex stretching and tilting effects, we now examine the general problem of vorticity generation in the idealized limit of zero bottom drag, and by implication, no bottom Ekman layer. From an oceanic perspective, this is an unphysical limit, yet a quantitative comparison with the drag solution serves to highlight by contrast the more robust features of BBL mediated vorticity generation.

Snapshots of the vertically integrated vorticity for the no-drag solutions (Figs. 11a–c) show that, after separation, the wake vortices have a smaller horizontal scale compared to the cases with drag at the same $\hat{h}$ (Fig. 1). As Ekman processes are absent, there are no submesoscale instabilities over the anticyclonic side of the ridge. The dominant source of vorticity production in these flows is advective vortex stretching and tilting. This is depicted in Figs. 12a–c. BSDT is negligibly small,

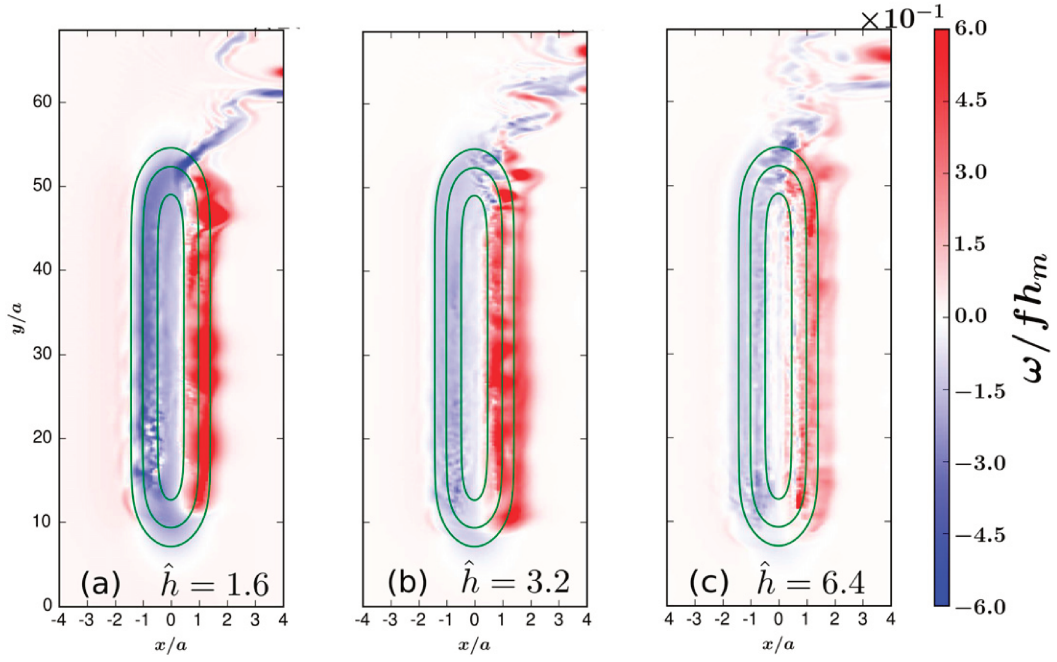

FIG. 11. Snapshots of vertically integrated vorticity, normalized by fh_m for solutions with no bottom drag: (a) $\hat{h} = 1.6$, (b) $\hat{h} = 3.2$, and (c) $\hat{h} = 6.4$. Compare with the drag solutions in Fig. 1.

so BPT is balanced purely by the inviscid terms in Eq. (11). Indeed, Fig. 12 reveals regions of partial overlap between VSVT and BPT. This must be contrasted with the drag cases (Fig. 10) in which BSDT was noted to be the dominant component of BPT. The disparate balances for flows with and without bottom drag show that, in realistic model solutions, the relative contributions of BSDT and advective processes to BPT are sensitive to the details of the drag parameterization and BBL resolution.

As in the drag solutions, we perform a quasi-Lagrangian integration of Eq. (18) along barotropic streamlines and average across many streamlines on either side of the ridge (Fig. 13a). Here we show the vortex stretching (VS) and tilting (VT) contributions separately rather than as a sum (VSVT). Note that while BSC is identically zero, BSDT is also practically negligible in these no-drag solutions (it is not identically zero because of the small background viscosity in ROMS). Figures 13b and 13c reveal that vorticity generation on both sides is attributable primarily to VT during the early flow encounter with the ridge. This is to be contrasted with the drag cases (Fig. 9) where vorticity is primarily generated by BSDT during the early encounter. An asymptotic analysis of the no-drag problem along the lines of Smolarkiewicz and Rotunno (1989) (see appendix) illustrates how a rotating, stratified flow encountering bottom topography causes tilting of horizontally oriented vortex tubes, generating vertical vorticity in the process.

On the anticyclonic side, we note an abrupt reversal in the tendencies of VS and VT just ahead of the straight ridge section. However, this does not produce any discernible change in the net vorticity, suggesting it represents merely a reversible, advective flow adjustment on the slopes rather than irreversible vorticity generation. Finally, here again, as in the drag solutions, there is negligible net generation of vorticity along the straight ridge section, where VS, VT, and eddy advection are approximately in balance.

That eddying solutions (Fig. 11) are obtained without bottom drag and BBL separation may seem surprising on the face of it. However, recall that although bottom drag is set to zero, these solutions are not truly inviscid. This is because of the biharmonic horizontal dissipation and mixing (Lemarié et al. 2012) implicit in the third-order upwind-biased scheme. As we shall see below, the eddies in Fig. 11 are in fact associated with potential vorticity (PV) anomalies.

We define the PV

$$q = \mathbf{\Omega}_a \cdot \nabla b \tag{25}$$

where $b = -g\rho/\rho_0$ is the buoyancy and $\mathbf{\Omega}_a$ is the three-dimensional absolute vorticity. The PV balance equation may be written in flux-divergence form as follows (e.g., Thomas 2005; McWilliams 2016),

$$\frac{\partial q}{\partial t} = -\nabla \cdot \left(\underbrace{q\mathbf{u}}_{\mathbf{J}_{\text{adv}}} + \underbrace{\nabla b \times \mathbf{F}}_{\mathbf{J}_V} - \underbrace{\mathscr{D}_b \mathbf{\Omega}_a}_{\mathbf{J}_B} \right). \tag{26}$$

Here ∇ is the three-dimensional gradient operator. The terms $\mathbf{J}_V$ and $\mathbf{J}_B$ denote viscous and diabatic fluxes of PV, respectively. The nonconservative terms are expressed concisely as

$$\mathbf{F} = \frac{\tau_z}{\rho_0} + D_h(\mathbf{u}) \tag{27a}$$

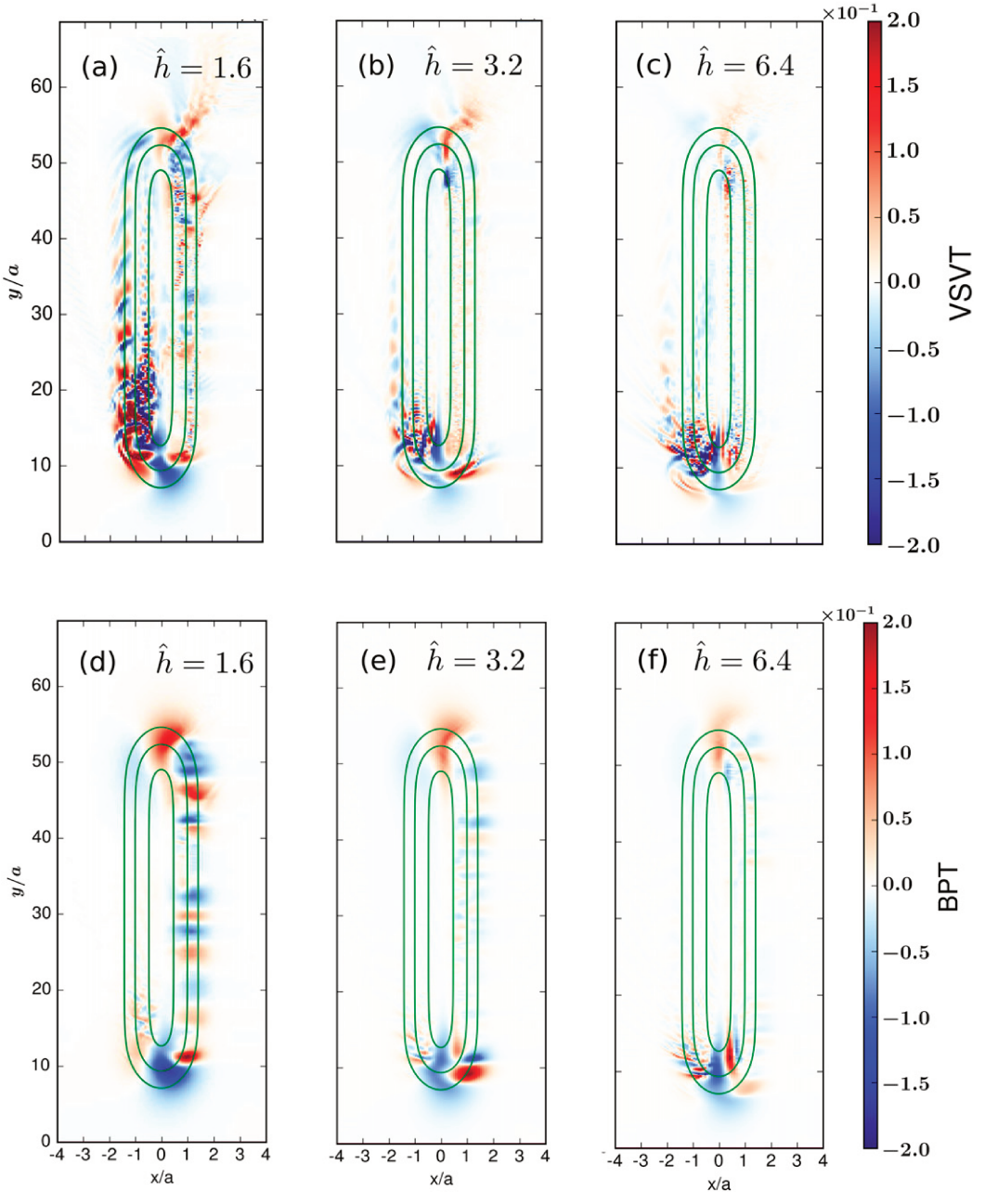

FIG. 12. (top) Time-averaged source term VSVT (sum of VS and VT) in Eq. (9) normalized by $fh_mV_0a^{-1}$ for the no-drag solutions. (bottom) Time-averaged bottom pressure torque (BPT), normalized by $fh_mV_0a^{-1}$. Values of the parameter $\hat{h}$ are indicated inside each panel.

$$\mathscr{D}_b = D_v(b) + D_h(b). \tag{27b}$$

where $D_v(b)$ is vertical divergence of the turbulent buoyancy flux and $D_h(\mathbf{u})$ and $D_h(b)$ represent horizontal momentum and buoyancy mixing, respectively.

In Fig. 14a, we display the PV, normalized by the background value fN^2 on the horizontal plane $z = -H + (h_m/2)$ for the case $\hat{h} = 3.2$. The figure reveals $\mathscr{O}(1)$ anomalies of PV in the wake vortices, implying a net flux of PV through the bottom boundary. As the bottom drag is identically zero by design, it follows that PV injection at the boundary can happen only due to the horizontal mixing terms. Indeed, we find that the PV flux through the topography $\mathbf{J}\cdot\hat{\mathbf{n}}$, where $\hat{\mathbf{n}}$ is the unit outward surface normal, is almost entirely due to the horizontal buoyancy mixing component $D_h(b)$ of the diabatic flux $\mathbf{J}_B$ (Fig. 14b), with both $\mathbf{J}_V$ and $D_v(b)$ being negligible in comparison. A possible interpretation is that horizontal buoyancy mixing leads to vertical shear (horizontal vorticity) generation

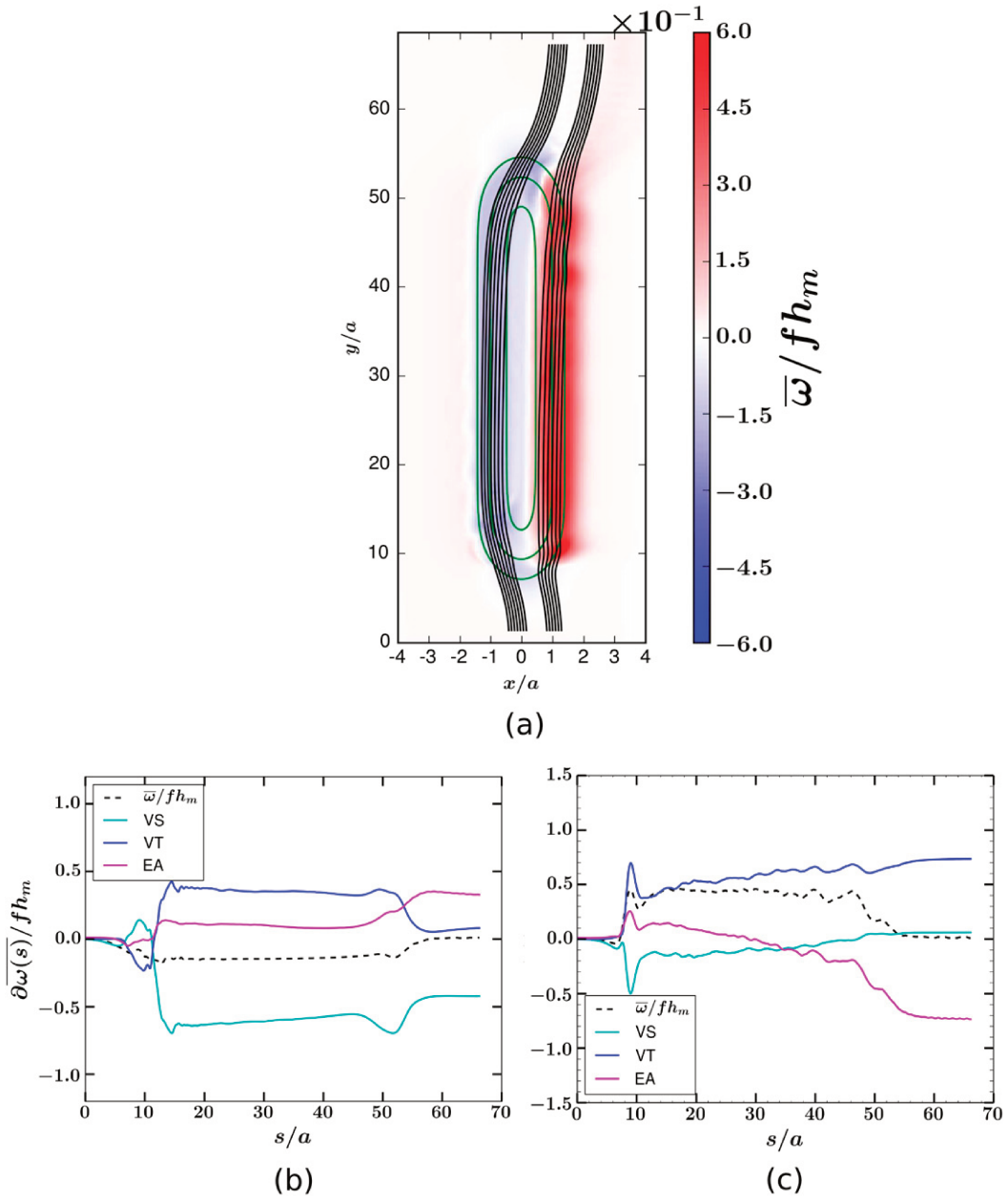

FIG. 13. (a) Time average of vertically integrated vorticity, normalized by fh_m for the $\hat{h} = 3.2$ no-drag solution. (bottom) As in Fig. 9, but for the no drag solution at $\hat{h} = 3.2$ for (b) anticyclonic side and (c) cyclonic side.

through the baroclinic torque, which is then tilted into the vertical during the topographic encounter. Hence, although frictional torques do not contribute directly to vertical vorticity generation in these no-drag solutions, the source of vorticity is ultimately nonconservative.

b. Comparison with the drag solutions

The qualitative differences between the drag and no-drag solutions are apparent when we compare snapshots like Fig. 1 with Fig. 11. To make more concrete these intuitive visual perspectives, we now examine some integral properties of the eddying flow. Following Srinivasan et al. (2019, 2021), eddy horizontal and vertical scales are defined as

$$\frac{1}{L_I} = \frac{1}{2\sqrt{2}}\frac{1}{T}\int_0^T \left[\frac{\int \zeta'^2\, dx\, dz}{\int \mathrm{EKE}\, dx\, dz}\right]^{1/2} dt, \tag{28a}$$

$$\frac{1}{H_I} = \frac{1}{2\sqrt{2}}\frac{1}{T}\int_0^T \left[\frac{\int U_z'^2\, dx\, dz}{\int \mathrm{EKE}\, dx\, dz}\right]^{1/2} dt. \tag{28b}$$

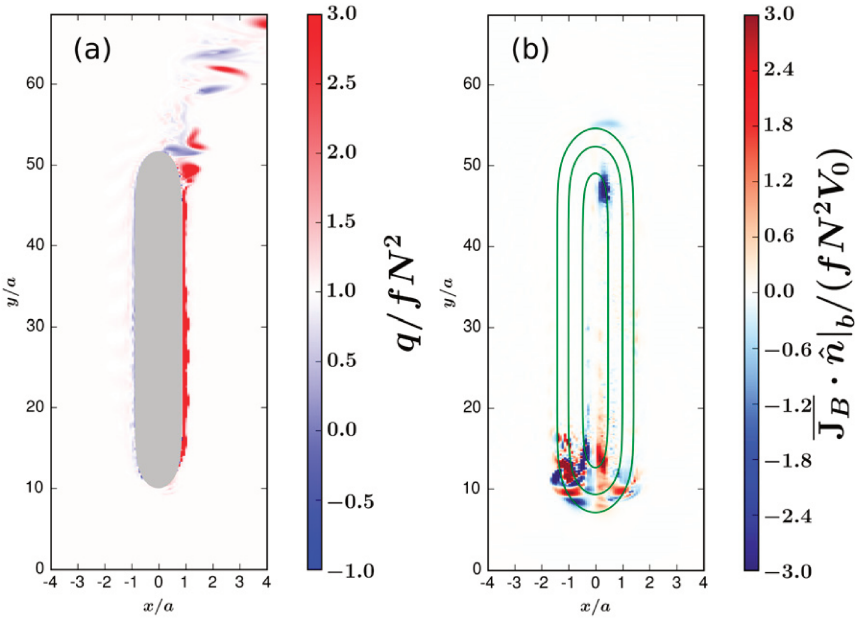

FIG. 14. PV and PV flux for the $\hat{h} = 3.2$, no-drag solution. (a) Snapshot of the PV normalized by the background value fN^2 on the horizontal plane $z = -H + (h_m/2)$ and (b) normalized, time-mean diabatic bottom flux of PV $(\overline{\mathbf{J}_B} \cdot \hat{\mathbf{n}})/(fN^2V_0)$ along the boundary normal $\hat{\mathbf{n}}$. Note that this is dominated by the horizontal buoyancy mixing component $D_h(b)\boldsymbol{\Omega}_a$.

Here EKE $= 0.5(u'^2 + v'^2)$ is the eddy kinetic energy, $\zeta'^2 = (v'_x - u'_y)^2$ is the eddy enstrophy, and $U'^2_z = 0.5(u'^2_z + v'^2_z)$ is the squared eddy vertical shear. All eddy quantities $(\,)'$ here are defined as deviations from a time mean $\overline{(\cdot)}$.

Figure 15 shows that the eddy integral scales in the no-drag cases do not depend sensitively on $\hat{h}$. The separated eddies have smaller horizontal scales than their drag counterparts. On the cyclonic side, the no-drag L_I are almost 60% smaller compared to the drag cases. Likewise, for $\hat{h} = 3.2$, the vertical eddy scales are also substantially smaller on either side of the ridge.

Another integral measure of SCV strength is its circulation,

$$\Gamma = \int_{\phi=0}^{2\pi} \int_{r=0}^{L_I} \omega' \, r \, dr \, d\phi, \tag{29}$$

where ω' is the vertically integrated eddy vorticity, with the origin taken to be the SCV center. The double integral is readily evaluated upon identifying the locations corresponding to the minima $\min_x[\min_y(\omega')]$ and maxima $\max_x[\max_y(\omega')]$ of ω' in the wake region.

Figures 17a and 17b display time averages over 50 inertial periods, $\overline{\Gamma_{\mathrm{AC}}}$ and $\overline{\Gamma_{\mathrm{CYC}}}$, respectively, of the anticyclonic and cyclonic SCVs in the wake. These have been normalized by $fh_m\pi a^2$, the strength of an axisymmetric columnar vortex of height h_m and radius a, with vorticity f at the center and a Gaussian radial distribution. There is only a weak $\hat{h}$ dependence of the SCV circulation $\overline{\Gamma}$ in the no-drag cases. Further, for a given value of $\hat{h}$, SCVs of either parity are stronger when bottom drag is included. For the anticyclonic SCVs, the ratio of their strengths with and without drag ranges from as large as 3.5 for $\hat{h} = 1.6$ to around 1.7 for $\hat{h} = 6.4$. The largest strength discrepancy (a factor greater than 3) in the case of the cyclonic SCVs is at $\hat{h} = 3.2$ and hovers around 2 for the other values of $\hat{h}$ considered.

To summarize, compared to the no-drag cases, bottom-drag-mediated vorticity generation spawns SCVs that are stronger and more energetic, and larger in scale, both horizontal and vertical.

6. Discussion and summary

Using idealized ROMS solutions and an integrated vorticity balance analysis, we have demonstrated the role of BBLs in mediating vorticity generation on ridge slopes when the nondimensional ridge height $\hat{h}$ is larger than 1. As a current encounters topography, the nonconservative frictional torque (BSDT), proportional to the vertical stress divergence on the slopes, injects vorticity into the flow. A quasi-Lagrangian analysis of the vertically integrated vorticity equation, Eq. (9) demonstrates that most of the vorticity injection happens during the early encounter with the ridge. The vorticity is intensified and redistributed in the interior through vortex stretching and tilting effects. The upshot of these processes is the emergence of vertically coherent vortices that eventually separate from the ridge slopes and roll up to form SCVs in the wake.

For all values of $\hat{h}$ considered, vorticity generation transpires primarily through the action of BSDT during the early encounter with the ridge, with the tendency terms largely being in a balanced state along the straight section of the ridge. For $\hat{h} \approx 6.4$ and higher, the stress reduction on the anticyclonic side

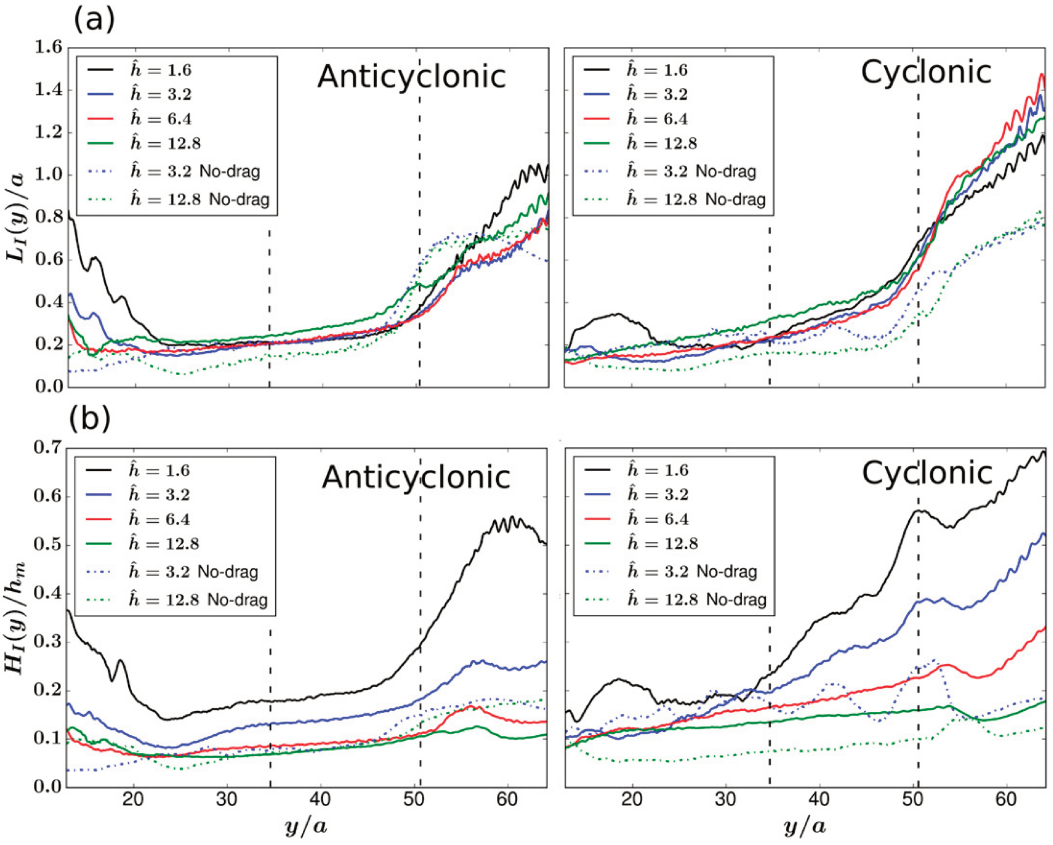

FIG. 15. Downstream evolution of eddy integral length scales [defined in Eq. (28)] on the cyclonic and anticyclonic sides for the ridge solutions (a) horizontal scale L_I/a and (b) vertical scale H_I/h_m. The dashed vertical lines mark the approximate locations of the ridge centerline and northern edge of the straight section.

is significant enough that, in a streamline-averaged sense, VSVT and BSDT reverse signs along the straight section of the ridge. However, as seen in Fig. 9, there is no net vorticity generation after this reversal occurs.

When the barotropic vorticity equation Eq. (22) is employed to analyze the vorticity balances, BPT is often interpreted as the inviscid twisting force responsible for steering flow around bottom topography (e.g., Jackson et al. 2006; Molemaker et al. 2015). However, because pressure is only a Lagrange multiplier when the incompressibility constraint is enforced, there is necessarily some ambiguity in its interpretation, particularly when viscous processes are involved. In the inviscid quasi-geostrophic limit, it is easily shown that BPT is exactly equal to bottom vortex stretching $-fw_b$. More generally, when expressed as a bottom momentum balance [Eq. (11)], BPT is seen to be directly related to both frictional (BSDT) and advective terms that account for the effects of bottom vortex stretching, tilting, and flow inertia. Indeed, as Fig. 10 demonstrates, in our solutions with a well-resolved BBL, the viscous torque BSDT is in fact the dominant component of BPT. These findings show that when BBLs are present, the apparently contradictory roles of BPT and BSDT in vorticity generation are only illusory. The advantage of the integrated vorticity formulation used here is that it explicitly eliminates the ambiguous pressure gradient term and partitions the generation into inviscid vortex stretching and tilting contributions and nonconservative boundary injection terms associated with the bottom drag.

Visually (e.g., Fig. 1), cyclones are at least as prevalent as anticyclones in our solutions, if not more so. Moreover, Fig. 17 shows that, by an average integral measure of circulation, cyclonic SCVs are in fact stronger than their anticyclonic counterparts. These results appear to contradict the fact that most observed SCVs in the ocean are anticyclonic—a theoretical puzzle that remains unresolved (McWilliams 1985, 2016). Recently, an intense cyclonic SCV has been documented in the Arabian Sea (De Marez et al. 2020), which the authors hypothesize has its origin at the mouth of the Gulf of Aden, a site of steep topography. More studies are needed to bridge the apparent gap between observations and simulations.

The alternating positive and negative patterns along the cyclonic slope in Figs. 12d and 12e for the no-drag case are reminiscent of the BPT signals around the Charleston Bump in the Gulf Stream simulation of Gula et al. (2015, their Fig. 13). This is consistent with their observation that bottom vortex stretching is locally the leading-order term in BPT around the Bump, implying a largely inviscid balance against the seaboard. In light of our results, it would appear that realistic simulations with higher BBL resolution are

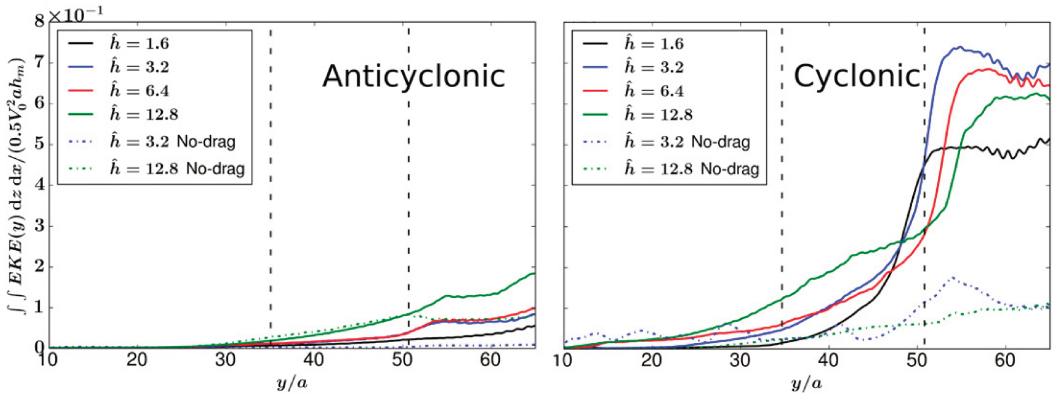

FIG. 16. Downstream evolution of the normalized, vertically integrated eddy kinetic energy on the anticyclonic and cyclonic sides for the ridge solutions. The dashed vertical lines mark the approximate locations of the ridge centerline and northern edge of the straight section.

needed to ascertain if the western boundary current truly represents an inviscid balance.

The importance of bottom drag in vorticity generation has been recognized previously, for example by Signell and Geyer (1991). Using a simple analytical model of flow separation and 2D simulations of the linearized, depth-averaged shallow water equations, they found that the choice of the drag coefficient strongly influenced eddy formation in tidally forced flows around headlands. In their formulation, the depth-averaged drag manifests through the so-called ''speed torque'' and ''slope torque'' terms. These may be considered roughly analogous to BSC and BSDT, respectively. A key difference is that while the Signell and Geyer (1991) model is 2D and moreover, relies on empirical choices for the depth averaged drag coefficient, here we directly demonstrate the role of BSDT in vorticity generation using three-dimensional ROMS simulations that resolve the BBL using the KPP parameterization.

Vorticity generation can happen even without bottom drag. The nonrotating, free-slip solutions of Smolarkiewicz and Rotunno (1989) are the earliest modeling evidence for this phenomenon. Recent work by Jagannathan et al. (2019) and Puthan et al. (2020), again for nonrotating flows, also show lee vortex formation with a free-slip bottom boundary. The present study demonstrates that vorticity generation without drag is possible in rotating systems as well, through vortex stretching and tilting mechanisms. However, as seen in Figs. 15–17, the wake eddies tend to be substantially less robust compared to the cases with bottom drag. Hence, model simulations that lack a bottom drag parameterization and/or insufficiently resolve the BBL will often tend to underestimate the spatial scales and strength of the SCVs, and care is needed in interpreting such solutions.

There are several outstanding issues. One question is, how do the dynamics differ for one-sided slopes vis-à-vis isolated topography, such as considered here? On isolated topography, it is conceivable that adverse pressure gradients resulting from the convex topographic curvature and horizontal around-ridge circulations influence boundary layer separation. This is certainly suggested by the analytical and two-dimensional model solutions of Signell and Geyer (1991) for flow around a headland, where the onset of flow separation is found to be controlled by a three-way balance between adverse pressure gradient, curvature, and drag effects. One-sided slopes are

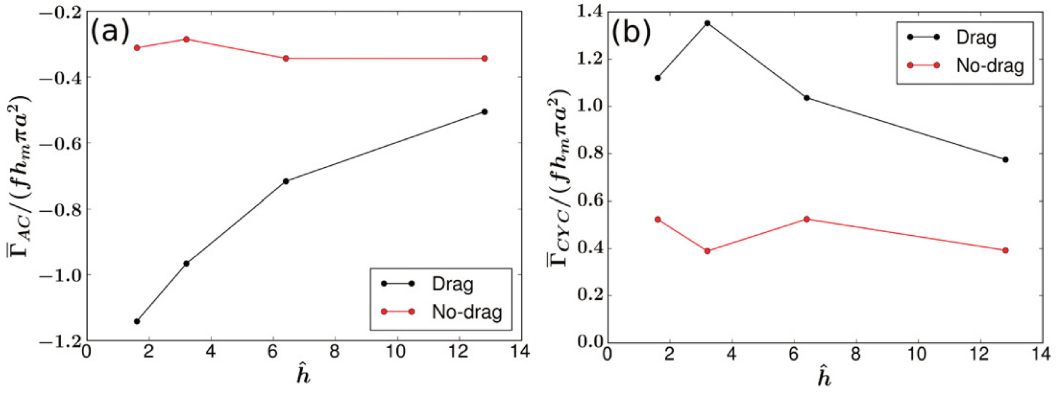

FIG. 17. The normalized, time-averaged circulation, defined in Eq. (29), of the wake SCVs for each of the drag and no-drag solutions: (a) anticyclonic circulation $\overline{\Gamma}_{AC}/(fh_m\pi a^2)$ and (b) cyclonic circulation $\overline{\Gamma}_{CYC}/(fh_m\pi a^2)$.

more directly relevant to boundary currents, and further understanding is needed there. Another pertinent question is, to what extent is Ekman arrest sensitive to ridge curvature and aspect ratio? Preliminary simulations also indicate that there is a transition from centrifugal to more strongly dissipative, hybrid centrifugal/symmetric instability as the ridge aspect ratio increases, i.e., it becomes more elongated. We will further explore some of these issues in a forthcoming paper.

Acknowledgments. This work was made possible by the Office of Naval Research Grant N00014-18-1-2599. Computing support was provided by the Extreme Science and Engineering Discovery Environment (XSEDE), which is supported by National Science Foundation Grant ACI-1548562. ALS was supported by the National Science Foundation under Grant OCE-1751386. We wish to thank Jacob Wenegrat for his insightful feedback on an early version of the draft.

APPENDIX

Asymptotic Analysis of the No-Drag Problem

The governing equations under the hydrostatic approximation are

$$\mathbf{u}\cdot\nabla_H u + w\frac{\partial u}{\partial z} - fv = -\frac{1}{\overline{\rho}}\frac{\partial p}{\partial x}, \tag{A1a}$$

$$\mathbf{u}\cdot\nabla_H v + w\frac{\partial v}{\partial z} + fu = -\frac{1}{\overline{\rho}}\frac{\partial p}{\partial y}, \tag{A1b}$$

$$\frac{\partial p}{\partial z} = -g\rho. \tag{A1c}$$

Along with this set of equations, we have the continuity equation

$$\nabla_H\cdot\mathbf{u} + \frac{\partial w}{\partial z} = 0, \tag{A2}$$

and the scalar advection equation

$$\mathbf{u}\cdot\nabla_H[\rho + \tilde{\rho}(z)] + w\frac{\partial\rho}{\partial z} + w\frac{\partial\tilde{\rho}(z)}{\partial z} = 0, \tag{A3}$$

where $\tilde{\rho}(z)$ is the background density field, assumed here to be uniformly stratified. For simplicity we impose rigid lid conditions $w = \rho = 0$ at the upper surface. Finally, in the absence of diapycnal fluxes, we can express the vertical velocity w in terms of the instantaneous isopycnal displacement field δ as

$$w = \mathbf{u}\cdot\nabla_H\delta. \tag{A4}$$

The boundary condition at the bottom $z_b = -H + h(x, y)$ is that of no flow into the topography

$$\mathbf{u}_b\cdot\nabla_H h = w_b. \tag{A5}$$

We nondimensionalize the various quantities as follows

$$(x', y') = (x, y)/a, \tag{A6}$$

$$z' = z/(afN^{-1}), \tag{A7}$$

$$(u', v') = (u, v)/(Nh_m), \tag{A8}$$

$$p' = p/(\overline{\rho}Nfh_m a), \tag{A9}$$

$$\rho' = \rho/(\overline{\rho}g^{-1}N^2h_m), \tag{A10}$$

$$\delta' = \delta/(afN^{-1}). \tag{A11}$$

Note that the scaling for p is chosen so that the leading-order balance is geostrophic. The appropriate choice of scale for the vertical velocity is constrained through the continuity equation as

$$w' = w/fh_m. \tag{A12}$$

The governing equations in dimensionless form are then given by (dropping primes),

$$\epsilon\left(\mathbf{u}\cdot\nabla_H u + w\frac{\partial u}{\partial z}\right) - v = -\frac{\partial p}{\partial x}, \tag{A13a}$$

$$\epsilon\left(\mathbf{u}\cdot\nabla_H v + w\frac{\partial v}{\partial z}\right) + u = -\frac{\partial p}{\partial y}, \tag{A13b}$$

$$\frac{\partial p}{\partial z} = -\rho, \tag{A13c}$$

$$\nabla_H\cdot\mathbf{u} + \frac{\partial w}{\partial z} = 0, \tag{A13d}$$

$$\mathbf{u}\cdot\nabla_H\rho + w\frac{\partial\rho}{\partial z} + w\frac{\partial\tilde{\rho}(z)}{\partial z} = 0. \tag{A13e}$$

Here $\epsilon = Nh_m/af = \hat{h}$ is the nondimensional ridge height. The bottom boundary condition is now given by

$$w_b = \epsilon\mathbf{u}_b\cdot\nabla_H h. \tag{A14}$$

Assuming $\epsilon < 1$, we now expand in powers of ϵ,

$$u = u_0 + \epsilon u_1 + \epsilon^2 u_2 + \mathcal{O}(\epsilon^3), \tag{A15}$$

and similarly for the other variables. Substituting these expansions in Eq. (A13), we have geostrophic balance at leading order,

$$v_0 = \frac{\partial p_0}{\partial x}, \tag{A16a}$$

$$u_0 = -\frac{\partial p_0}{\partial y}. \tag{A16b}$$

The continuity equation and the boundary condition $w_0 = 0$ on the upper surface then leads to

$$\partial w_0/\partial z = w_0 = \rho_0 = 0. \tag{A17}$$

Therefore at leading order, the streamlines and hence isopycnals lie on horizontal planes. Geostrophic balance and the hydrostatic approximation Eq. (A13d) then imply that the vertical gradients of u, v, and ρ are all zero and the flow is essentially barotropic.

The $\mathcal{O}(\epsilon)$ balance is given by

$$u_0\frac{\partial u_0}{\partial x} + v_0\frac{\partial u_0}{\partial y} - v_1 = -\frac{\partial p_1}{\partial x}, \tag{A18a}$$

$$u_0\frac{\partial v_0}{\partial x}+v_0\frac{\partial v_0}{\partial y}+u_1=-\frac{\partial p_1}{\partial y}. \tag{A18b}$$

Taking cross derivatives with respect to x and y and subtracting Eq. (A18a) from (A18b),

$$\mathbf{u}_0\cdot\nabla_H\zeta_0=\frac{\partial w_1}{\partial z}. \tag{A19}$$

Equation (A19) tells us that the vertical vorticity at $\mathcal{O}(1)$, $\zeta_0=\partial v_0/\partial x-\partial u_0/\partial y$ arises purely as a consequence of linear vortex stretching at $\mathcal{O}(\epsilon)$. This is the quasigeostrophic limit explored by Hogg (1973) and Schär and Davies (1988), among others, which predicts a conical anticyclone on top of the seamount.

The $\mathcal{O}(\epsilon^2)$ problem

At this order, the horizontal momentum equations are

$$u_0\frac{\partial u_1}{\partial x}+v_0\frac{\partial u_1}{\partial y}+u_1\frac{\partial u_0}{\partial x}+v_1\frac{\partial u_0}{\partial y}+w_1\cancel{\frac{\partial u_0}{\partial z}}^{0}-v_2=-\frac{\partial p_2}{\partial x}, \tag{A20a}$$

$$u_0\frac{\partial v_1}{\partial x}+v_0\frac{\partial v_1}{\partial y}++u_1\frac{\partial v_0}{\partial x}+v_1\frac{\partial v_0}{\partial y}+w_1\cancel{\frac{\partial v_0}{\partial z}}^{0}+u_2=-\frac{\partial p_2}{\partial y}. \tag{A20b}$$

Cross differentiating and subtracting as before,

$$\mathbf{u}_0\cdot\nabla_H\zeta_1=-\mathbf{u}_1\cdot\nabla_H\zeta_0+\underbrace{\zeta_0\frac{\partial w_1}{\partial z}}_{\text{QL VS}}+\underbrace{\frac{\partial w_2}{\partial z}}_{\text{linear }\mathcal{O}(\epsilon^2)\text{ VS}}. \tag{A21}$$

Thus at $\mathcal{O}(\epsilon)$, a cross term appears that is quasi linear at $\mathcal{O}(\epsilon)$. This term represents stretching of $\mathcal{O}(1)$ vorticity by the $\mathcal{O}(\epsilon)$ horizontal divergence.

The $\mathcal{O}(\epsilon^3)$ problem

$$u_1\frac{\partial u_1}{\partial x}+v_1\frac{\partial u_1}{\partial y}+w_1\frac{\partial u_1}{\partial z}+u_0\frac{\partial u_2}{\partial x}+v_0\frac{\partial u_2}{\partial y}+u_2\frac{\partial u_0}{\partial x}+v_2\frac{\partial u_0}{\partial y}-v_3=-\frac{\partial p_3}{\partial x}, \tag{A22a}$$

$$u_1\frac{\partial v_1}{\partial x}+v_1\frac{\partial v_1}{\partial y}+w_1\frac{\partial v_1}{\partial z}+u_0\frac{\partial v_2}{\partial x}+v_0\frac{\partial v_2}{\partial y}+u_2\frac{\partial v_0}{\partial x}+v_2\frac{\partial v_0}{\partial y}+u_3=-\frac{\partial p_3}{\partial y}. \tag{A22b}$$

Cross differentiating and subtracting as before,

$$\mathbf{u}_0\cdot\nabla_H\zeta_2=-\mathbf{u}_1\cdot\nabla_H\zeta_1+\underbrace{\zeta_1\frac{\partial w_1}{\partial z}+\zeta_0\frac{\partial w_2}{\partial z}}_{\text{NL VS}}+\underbrace{\frac{\partial w_3}{\partial z}}_{\text{linear }\mathcal{O}(\epsilon^3)\text{ VS}}+\underbrace{\xi_1\frac{\partial w_1}{\partial x}+\eta_1\frac{\partial w_1}{\partial y}}_{\text{tilting of }0(\epsilon)\text{ horz. vorticity}}, \tag{A23}$$

where $\xi_1=\partial v_1/\partial z$ and $\eta_1=\partial u_1/\partial z$ are the two components of $\mathcal{O}(\epsilon)$ horizontal vorticity. Thus at $\mathcal{O}(\epsilon^2)$, in addition to linear and nonlinear vortex stretching, vortex tilting effects start to become important in determining the vertical vorticity evolution. Now under the hydrostatic approximation, the horizontal vorticity is identical to the vertical shear. At $\mathcal{O}(\epsilon)$, the equations for vertical shear are obtained by taking the derivatives with respect to z of Eqs. (A18a) and (A18b). Recalling that $(\partial u_0/\partial z)=(\partial v_0/\partial z)=0$ and using the hydrostatic pressure equation Eq. (A13d) to eliminate p_1, we have,

$$\xi_1=-\frac{\partial v_1}{\partial z}=-\frac{\partial}{\partial x}\left(\frac{\partial p_1}{\partial z}\right)=\frac{\partial \rho_1}{\partial x}, \tag{A24a}$$

$$\eta_1=\frac{\partial u_1}{\partial z}=-\frac{\partial}{\partial y}\left(\frac{\partial p_1}{\partial z}\right)=\frac{\partial \rho_1}{\partial y}. \tag{A24b}$$

The parity of ξ_1 and η_1 can be inferred from consideration of the $\mathcal{O}(\epsilon)$ scalar advection equation, Eq. (A13e),

$$\mathbf{u}_0\cdot\nabla_H\rho_1+w_1\frac{\partial\tilde{\rho}}{\partial z}=0. \tag{A25}$$

Using Eq. (A4) w_1 can be expressed in terms of the isopycnal displacement field δ_1 as

$$w_1=\mathbf{u}_0\cdot\nabla_H\delta_1. \tag{A26}$$

Close to the bottom, we can further use the boundary condition of no normal flow into the topography [Eq. (A14)] to approximate w_1 as $w_1\approx\mathbf{u}_0\cdot\nabla_H h$. Then, Eq. (A25) can be written as

$$\mathbf{u}_0\cdot\nabla_H\left(\rho_1+h\frac{\partial\tilde{\rho}}{\partial z}\right)=0. \tag{A27}$$

Equation (A27) tells us that $(\rho_1+h\partial\tilde{\rho}/\partial z)$ remains constant on the $\mathcal{O}(1)$ horizontal streamlines of the flow. Now noting that $\partial\tilde{\rho}/\partial z<0$ for a stably stratified background, this implies that the two components of $\nabla_H\rho_1$ near the bottom have the same parity, respectively, as those of $\nabla_H h$. In the context of our ridge solutions (e.g., Fig. 11), Eq. (A24) shows that as the flow encounters the ridge, $\xi_1<0$ (>0) on the cyclonic (anticyclonic) side, while $\eta_1>0$ on both sides.

Therefore, when $\epsilon=Nh_m/(fa)$ is not asymptotically small, second-order nonlinear effects are important from the perspective of vorticity production. While the perturbation analysis above does not automatically carry over to the cases $\hat{h}>1$ which we consider, it does nevertheless show that nonlinear vortex stretching and tilting effects can be significant away from the quasigeostrophic limit. Note that the analysis presented here differs from the nonrotating case considered by Smolarkiewicz and Rotunno (1989) in which the appropriate small parameter is the inverse Froude number $\mathrm{Fr}^{-1}=Nh_m/V_0$. In that case, the $\mathcal{O}(1)$ and $\mathcal{O}(\mathrm{Fr}^{-1})$ contributions are both uniformly zero and the vertical vorticity, which is generated by tilting of baroclinically generated $\mathcal{O}(\mathrm{Fr}^{-1})$ horizontal vorticity, makes an appearance only at $\mathcal{O}(\mathrm{Fr}^{-2})$.

REFERENCES

Armi, L., and H. Stommel, 1983: Four views of a portion of the North Atlantic subtropical gyre. *J. Phys. Oceanogr.*, **13**, 828–857, https://doi.org/10.1175/1520-0485(1983)013<0828:FVOAPO>2.0.CO;2.

——, and W. Zenk, 1984: Large lenses of highly saline Mediterranean water. *J. Phys. Oceanogr.*, **14**, 1560–1576, https://doi.org/10.1175/1520-0485(1984)014<1560:LLOHSM>2.0.CO;2.

Baines, P. G., 1998: *Topographic Effects in Stratified Flows*. Cambridge University Press, 482 pp.

Benthuysen, J., and L. N. Thomas, 2012: Friction and diapycnal mixing at a slope: Boundary control of potential vorticity. *J. Phys. Oceanogr.*, **42**, 1509–1523, https://doi.org/10.1175/JPO-D-11-0130.1.

Brink, K. H., and S. J. Lentz, 2010: Buoyancy arrest and bottom Ekman transport. Part I: Steady flow. *J. Phys. Oceanogr.*, **40**, 621–635, https://doi.org/10.1175/2009JPO4266.1.

Capó, E., J. C. McWilliams, E. Mason, and A. Orfila, 2021: Intermittent frontogenesis in the Alboran Sea. *J. Phys. Oceanogr.*, **51**, 1417–1439, https://doi.org/10.1175/JPO-D-20-0277.1.

D'Asaro, E. A., 1988: Generation of submesoscale vortices: A new mechanism. *J. Geophys. Res.*, **93**, 6685–6693, https://doi.org/10.1029/JC093iC06p06685.

De Marez, C., X. Carton, S. Corréard, P. L'Hégaret, and M. Morvan, 2020: Observations of a deep submesoscale cyclonic vortex in the Arabian Sea. *Geophys. Res. Lett.*, **47**, e2020GL087881, https://doi.org/10.1029/2020GL087881.

Dewar, W., J. McWilliams, and M. Molemaker, 2015: Centrifugal instability and mixing in the California Undercurrent. *J. Phys. Oceanogr.*, **45**, 1224–1241, https://doi.org/10.1175/JPO-D-13-0269.1.

Garrett, C., P. MacCready, and P. Rhines, 1993: Boundary mixing and arrested Ekman layers: Rotating stratified flow near a sloping boundary. *Annu. Rev. Fluid Mech.*, **25**, 291–323, https://doi.org/10.1146/annurev.fl.25.010193.001451.

Gula, J., M. Molemaker, and J. McWilliams, 2015: Topographic vorticity generation, submesoscale instability and vortex street formation in the Gulf Stream. *Geophys. Res. Lett.*, **42**, 4054–4062, https://doi.org/10.1002/2015GL063731.

Hogg, N. G., 1973: On the stratified Taylor column. *J. Fluid Mech.*, **58**, 517–537, https://doi.org/10.1017/S0022112073002302.

Hughes, C. W., and B. A. De Cuevas, 2001: Why western boundary currents in realistic oceans are inviscid: A link between form stress and bottom pressure torques. *J. Phys. Oceanogr.*, **31**, 2871–2885, https://doi.org/10.1175/1520-0485(2001)031<2871:WWBCIR>2.0.CO;2.

Jackett, D. R., and T. J. McDougall, 1995: Minimal adjustment of hydrographic profiles to achieve static stability. *J. Atmos. Oceanic Technol.*, **12**, 381–389, https://doi.org/10.1175/1520-0426(1995)012<0381:MAOHPT>2.0.CO;2.

Jackson, L., C. W. Hughes, and R. G. Williams, 2006: Topographic control of basin and channel flows: The role of bottom pressure torques and friction. *J. Phys. Oceanogr.*, **36**, 1786–1805, https://doi.org/10.1175/JPO2936.1.

Jagannathan, A., K. B. Winters, and L. Armi, 2019: Stratified flows over and around long dynamically tall mountain ridges. *J. Atmos. Sci.*, **76**, 1265–1287, https://doi.org/10.1175/JAS-D-18-0145.1.

Large, W. G., J. C. McWilliams, and S. C. Doney, 1994: Oceanic vertical mixing: A review and a model with a nonlocal boundary layer parameterization. *Rev. Geophys.*, **32**, 363–403, https://doi.org/10.1029/94RG01872.

Lemarié, F., J. Kurian, A. F. Shchepetkin, M. J. Molemaker, F. Colas, and J. C. McWilliams, 2012: Are there inescapable issues prohibiting the use of terrain-following coordinates in climate models? *Ocean Modell.*, **42**, 57–79, https://doi.org/10.1016/j.ocemod.2011.11.007.

MacCready, P., and P. B. Rhines, 1991: Buoyant inhibition of Ekman transport on a slope and its effect on stratified spin-up. *J. Fluid Mech.*, **223**, 631–661, https://doi.org/10.1017/S0022112091001581.

MacKinnon, J. A., M. H. Alford, G. Voet, K. L. Zeiden, T. S. Johnston, M. Siegelman, S. Merrifield, and M. Merrifield, 2019: Eddy wake generation from broadband currents near Palau. *J. Geophys. Res. Oceans*, **124**, 4891–4903, https://doi.org/10.1029/2019JC014945.

Marchesiello, P., J. C. McWilliams, and A. Shchepetkin, 2001: Open boundary conditions for long-term integration of regional oceanic models. *Ocean Modell.*, **3**, 1–20, https://doi.org/10.1016/S1463-5003(00)00013-5.

McCoy, D., D. Bianchi, and A. L. Stewart, 2020: Global observations of submesoscale coherent vortices in the ocean. *Prog. Oceanogr.*, **189**, 102452, https://doi.org/10.1016/j.pocean.2020.102452.

McWilliams, J. C., 1985: Submesoscale, coherent vortices in the ocean. *Rev. Geophys.*, **23**, 165–182, https://doi.org/10.1029/RG023i002p00165.

——, 2016: Submesoscale currents in the ocean. *Proc. Roy. Soc.*, **472A**, 20160117, https://doi.org/10.1098/rspa.2016.0117.

——, E. Huckle, and A. F. Shchepetkin, 2009: Buoyancy effects in a stratified Ekman layer. *J. Phys. Oceanogr.*, **39**, 2581–2599, https://doi.org/10.1175/2009JPO4130.1.

Molemaker, M. J., J. C. McWilliams, and W. K. Dewar, 2015: Submesoscale instability and generation of mesoscale anticyclones near a separation of the California Undercurrent. *J. Phys. Oceanogr.*, **45**, 613–629, https://doi.org/10.1175/JPO-D-13-0225.1.

Ólafsson, H., and P. Bougeault, 1996: Nonlinear flow past an elliptic mountain ridge. *J. Atmos. Sci.*, **53**, 2465–2489, https://doi.org/10.1175/1520-0469(1996)053<2465:NFPAEM>2.0.CO;2.

Puthan, P., M. Jalali, J. L. Ortiz-Tarin, K. Chongsiripinyo, G. Pawlak, and S. Sarkar, 2020: The wake of a three-dimensional underwater obstacle: Effect of bottom boundary conditions. *Ocean Modell.*, **149**, 101611, https://doi.org/10.1016/j.ocemod.2020.101611.

Riser, S. C., W. B. Owens, H. T. Rossby, and C. C. Ebbesmeyer, 1986: The structure, dynamics, and origin of a small-scale lens of water in the western North Atlantic thermocline. *J. Phys. Oceanogr.*, **16**, 572–590, https://doi.org/10.1175/1520-0485(1986)016<0572:TSDAOO>2.0.CO;2.

Ruan, X., A. F. Thompson, and J. R. Taylor, 2019: The evolution and arrest of a turbulent stratified oceanic bottom boundary layer over a slope: Downslope regime. *J. Phys. Oceanogr.*, **49**, 469–487, https://doi.org/10.1175/JPO-D-18-0079.1.

Schär, C., 2002: Mesoscale mountains and the larger-scale atmospheric dynamics: A review. *Int. Geophys.*, **83**, 29–42, https://doi.org/10.1016/S0074-6142(02)80155-3.

——, and H. C. Davies, 1988: Quasi-geostrophic stratified flow over isolated finite amplitude topography. *Dyn. Atmos. Oceans*, **11**, 287–306, https://doi.org/10.1016/0377-0265(88)90003-6.

Shchepetkin, A. F., and J. C. McWilliams, 2003: A method for computing horizontal pressure-gradient force in an oceanic model with a nonaligned vertical coordinate. *J. Geophys. Res.*, **108**, 3090, https://doi.org/10.1029/2001JC001047.

——, and ——, 2005: The Regional Oceanic Modeling System (ROMS): A split-explicit, free-surface, topography-following-coordinate oceanic model. *Ocean Modell.*, **9**, 347–404, https://doi.org/10.1016/j.ocemod.2004.08.002.

Signell, R. P., and W. R. Geyer, 1991: Transient eddy formation around headlands. *J. Geophys. Res.*, **96**, 2561–2575, https://doi.org/10.1029/90JC02029.

Smolarkiewicz, P. K., and R. Rotunno, 1989: Low Froude number flow past three-dimensional obstacles. Part I: Baroclinically generated lee vortices. *J. Atmos. Sci.*, **46**, 1154–1164, https://doi.org/10.1175/1520-0469(1989)046<1154:LFNFPT>2.0.CO;2.

Srinivasan, K., J. C. McWilliams, L. Renault, H. G. Hristova, J. Molemaker, and W. S. Kessler, 2017: Topographic and mixed layer submesoscale currents in the near-surface southwestern tropical Pacific. *J. Phys. Oceanogr.*, **47**, 1221–1242, https://doi.org/10.1175/JPO-D-16-0216.1.

——, ——, M. J. Molemaker, and R. Barkan, 2019: Submesoscale vortical wakes in the lee of topography. *J. Phys. Oceanogr.*, **49**, 1949–1971, https://doi.org/10.1175/JPO-D-18-0042.1.

——, ——, and A. Jagannathan, 2021: High vertical shear and dissipation in equatorial topographic wakes. *J. Phys. Oceanogr.*, https://doi.org/10.1175/JPO-D-20-0119.1, in press.

Thomas, L. N., 2005: Destruction of potential vorticity by winds. *J. Phys. Oceanogr.*, **35**, 2457–2466, https://doi.org/10.1175/JPO2830.1.

Vic, C., G. Roullet X. Capet, X. Carton, M. J. Molemaker, and J. Gula, 2015: Eddy-topography interactions and the fate of the Persian Gulf outflow. *J. Geophys. Res. Oceans*, **120**, 6700–6717, https://doi.org/10.1002/2015JC011033.

Wenegrat, J. O., and L. N. Thomas, 2017: Ekman transport in balanced currents with curvature. *J. Phys. Oceanogr.*, **47**, 1189–1203, https://doi.org/10.1175/JPO-D-16-0239.1.

——, and ——, 2020: Centrifugal and symmetric instability during Ekman adjustment of the bottom boundary layer. *J. Phys. Oceanogr.*, **50**, 1793–1812, https://doi.org/10.1175/JPO-D-20-0027.1.

Zhang, Z., Z. Liu, K. Richards, G. Shang, W. Zhao, J. Tian, X. Huang, and C. Zhou, 2019: Elevated diapycnal mixing by a subthermocline eddy in the western equatorial Pacific. *Geophys. Res. Lett.*, **46**, 2628–2636, https://doi.org/10.1029/2018GL081512.